INVERSION OF COMBINED GEOPHYSICAL DATA FOR DETERMINATION OF STRUCTURE BENEATH THE IMPERIAL VALLEY GEOTHERMAL REGION

Final Report

By
J. M. Savino
W. L. Rodi
R. C. Goff
T. H. Jordan
J. H. Alexander
D. G. Lambert

September 1977

Systems, Science and Software
La Jolla, California

U. S. DEPARTMENT OF ENERGY

Geothermal Energy

SSS-R-78-3412

SYSTEMS, SCIENCE AND SOFTWARE

INVERSION OF COMBINED GEOPHYSICAL DATA FOR DETERMINATION OF STRUCTURE BENEATH THE IMPERIAL VALLEY GEOTHERMAL REGION

FINAL REPORT

1 September 1976 - 31 August 1977

J. M. SAVINO
W. L. RODI
R. C. GOFF
T. H. JORDAN
J. H. ALEXANDER
D. G. LAMBERT

SEPTEMBER 1977

P. O. BOX 1620, LA JOLLA, CALIFORNIA 92038

TABLE OF CONTENTS

TABLE OF CONTENTS (continued)

LIST OF ILLUSTRATIONS

iv

LIST OF ILLUSTRATIONS (continued)

LIST OF ILLUSTRATIONS (continued)

I. PROGRAM SUMMARY

1.1   PROGRAM OBJECTIVES

Geophysical exploration, as it is most commonly practiced, involves the measurement of several different parameters on the earth's surface and, at most, a semi-quantitative joint interpretation of the resulting information for subsurface structure. While this traditional approach has met with considerable success, by not simultaneously modeling the different data sets it fails to take advantage of all the available information, in particular the different spatial dependencies and tradeoffs inherent in the field measurements.

In an attempt to improve on the traditional approach to exploration and in view of recent advances in geophysical modeling procedures, namely general linear inversion, we undertook a program aimed at developing formal numerical modeling techniques that are applicable to combined geophysical data sets for defining the earth's near surface environment. Specific objectives of this program involved the development of forward and generalized inverse modeling techniques and their application to data obtained in a geothermal region for reservoir delineation and assessment. The results of this one-year effort point up the increased structural resolution afforded by this approach.

The numerical modeling procedures that have been developed are generally applicable to a variety of geophysical measurements (i.e., gravity, magnetotelluric, teleseismic travel-times and local earthquake arrival times and amplitudes). Given a functional relationship between the different parameters that are measured in the field, we are now in a position to carry out a simultaneous inversion of any number of geophysical data sets. The strategy adopted during the first year of this program was to attempt a joint inversion using

1

two of the most commonly acquired data sets for which a functional relationship can be assumed; gravity and teleseismic travel-times. In this case the parameters of interest are $\Delta\rho$, variations in density, and Δa, variations in slowness, where $\Delta\rho = f(\Delta a)$. The test region chosen for our initial modeling experiment is the Imperial Valley, California; an area of proven geothermal resources.

1.2 PROGRAM STRUCTURE AND REPORT ORGANIZATION

The research program consisted of five main steps:

1. Acquisition and processing of teleseismic travel-time and gravity data for the Imperial Valley.

2. Development and testing of forward modeling routines; procedures for calculating travel-times and the gravity field for various three-dimensional velocity and density structures.

3. Generation of a velocity and density model for the near-surface sedimentary layers in the Imperial Valley and subtraction (stripping) of the contributions due to the sediments from the seismic and gravity data sets.

4. Development of joint inversion techniques and their application to combined teleseismic and gravity data for obtaining a three-dimensional geologically consistent model of the subsurface physical properties; density and compressional wave velocity.

5. Interpretation of the model in light of known
       geological and geothermal features.

    Steps 1 through 3 were carried out during the first
nine months of this program and have been described in detail
in a series of quarterly reports written under this contract
(Savino, et al., 1976; Savino, et al., March 1977; Savino,
et al., June 1977). For the sake of making this report self-
contained, however, we will briefly summarize the most impor-
tant results of these three steps in later sections.

    During the last three months of this program, our
efforts concentrated on Steps 4 and 5. The numerical modeling
procedures developed and results obtained in these areas form
the bulk of this report and are described in Sections II and
III, respectively. Our conclusions are enumerated in Section
IV. For the benefit of those with only limited interest in
the program details, we will summarize the most important
results of the modeling experiment for the Imperial Valley
in the remainder of this section.

1.3   GEOLOGIC AND TECTONIC SETTING OF TEST REGION

    The region chosen for a proof-test of the numerical
modeling techniques includes the southern portion of the
physiographic province known as the Salton Basin (Figure 1).
This basin is the surface expression of a deep, sediment-
filled, structural trough, or rift valley, called the Salton
Trough which is considered to be the landward extension of
the Gulf of California. The trough encompasses the low-lying
areas of the Colorado River delta region in Mexico and the
Imperial Valley situated between the Peninsular Ranges of
coastal Southern California to the west and the Chocolate
Mountains to the east.

    The Gulf of California and the Salton Trough are areas
of rapid tectonic deformation, where patterns of high seismic-
ity and high heat flow, together with patterns of sedimentation

3
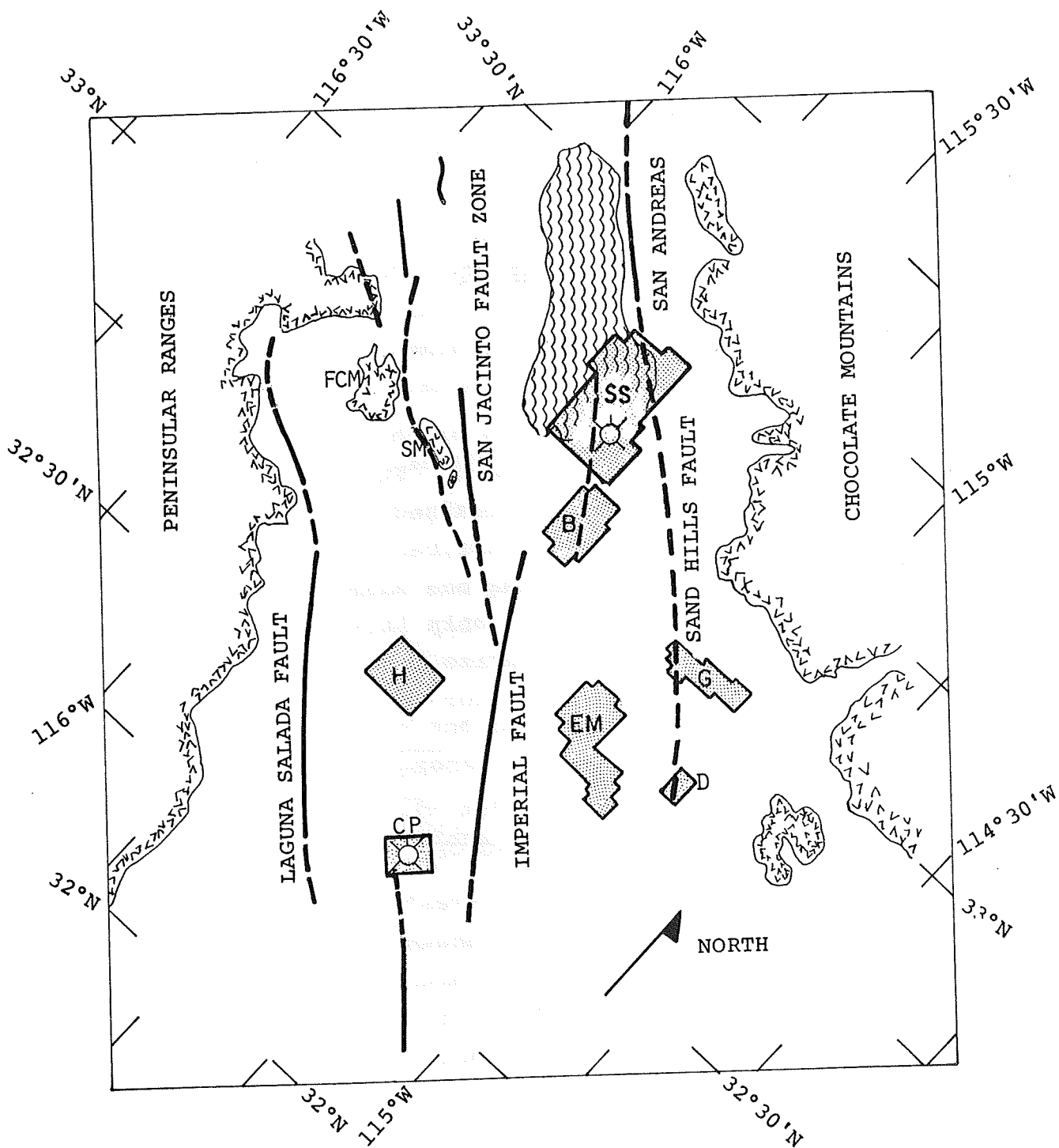
Figure 1. Map of the test region examined in this study. The major fault zones are given by the heavy solid and dashed lines. The geothermal areas (KGRA's) are as follows: SS = Salton Sea, B = Brawley, H = Heber, EM = East Mesa, D = Dunes, G = Glamis and CP = Cerro Prieto. The symbol ⊗ identifies volcanoes near the southeastern edge of the Salton Sea and Cerro Prieto. The features labeled FCM and SM are Fish Creek Mountain and Superstition Mountain, respectively.

4

and volcanicity, reflect a transition from the divergent plate boundary of the East Pacific Rise to the transform boundary represented by the San Andreas fault system (Wilson, 1965; Larson, et al., 1968; Atwater, 1970; Elders, et al., 1972). The formation of the Salton Trough is thought to be the result of a combination of tensional and right-lateral strike-slip movements associated with the opening of the Gulf of California. Elders, et al., (1972) have proposed a model in which the continental crust is being thinned beneath a deepening and widening rift. Dilation is accompanied by high heat flow and magmatism. The trough forms as successive sections of the crust are sliced off along strike-slip faults. These slices move northwest and are transferred from the North American to the Pacific plate.

The tectonic pattern of the northern Gulf of California and Salton trough has many features of a simple system of transform faults connected by ridge segments (Lomnitz, et al., 1970). Referring to Figure 1, several of the transform faults in this region (San Andreas-Sand Hills, Brawley, Imperial and San Jacinto) are seen as fairly straight features ending abruptly with neither geologic nor seismic evidence of continuation, at regions which may be inferred to be spreading centers (i.e., ridge segments). Evidence for the spreading centers includes geothermal steam fields, young volcanic activity, and the occurrence of earthquake swarms. In particular, both of the Known Geothermal Resource Areas (KGRA's) at Cerro Prieto and the Salton Buttes are located near the intersections of transform faults with a suspected ridge segment (e.g., the KGRA at Cerro Prieto is located on a ridge segment between the San Jacinto and Imperial faults).

Several other KGRA's have been identified in the Imperial Valley (Figure 1) on the basis of heat flow measurements and gravity anomalies (Elders, et al., 1972). These include East Mesa, Glamis, Dunes, Heber and Brawley. In

contrast to Cerro Prieto and the Salton Buttes, however, there
is no surface expression of the thermal anomalies at these
other KGRA's; such as warm springs, mud pots and quaternary
volcanoes. Thus, one of the objectives of our modeling experi-
ment was to use teleseismic travel-times and gravity observa-
tions to define the subsurface three-dimensional density and
velocity structure of this region in an attempt to identify the
sources of the geothermal reservoirs.

1.4   DESCRIPTION OF RESULTS

The teleseismic data base compiled for this experiment
was obtained from seismograms for worldwide earthquakes re-
corded at one or more of the 16 stations of the USGS-Caltech
network operating in the Imperial Valley. Several thousand
time picks were made for different portions of the P waves
from 182 events that occurred during the three year interval
April 1973 to July 1976. The data were grouped according to
event source region, corrected for estimates of delays due
to the sediment stack in the Imperial Valley and zero-meaned
to minimize contributions from deep structures (i.e., > 50 km).

The gravity data were supplied by Professor Shawn
Biehler of the University of California at Riverside. This
data base consisted of 13,715 observations, with complete
Bouguer corrections, for the region 32° to 34°N, 114° to 117°W.
These data were fit with a quadratic surface and interpolated
to a regular grid. Subsequent processing included various
filtering, stripping for the effects of the sedimentary layers
and decimation. An important last step in the processing pro-
cedure was to rotate the observed travel-time and gravity data
sets by 45 degrees into a coordinate system more nearly aligned
with the prevailing northwest trend of geologic features in the
test region. The configuration of the seismic array, the
spatial coverage of the gravity observations and the processing
of both data sets are described in detail in Section III.

6

A simultaneous inversion of the combined travel-time
and gravity data was carried out. In this calculation we
modeled the crust and topmost mantle in the region shown in
Figure 1 as a four layer cell model, each layer consisting
of an eight by nine grid of cells. Lateral variations in
density and slowness were assumed to exist only between 6 and
33 km, except for the sedimentary section in the upper 6 km
for which both the travel-time delays and gravity data were
corrected. A linear density-velocity relationship (Press
and Biehler, 1964) was assumed for each layer in the inversion.

One of the more important points concluded from the
inversion calculation was that lateral density and velocity
contrasts needed to fit the observed data were quite large:
greater than 0.3 gm/cc and 0.75 km/s, respectively. These
large contrasts were assumed to be due to the difference be-
tween crust and mantle materials. Thus, the most likely expla-
nation for most of the observed gravity and travel-time anomalies
was considered to be lateral variations in crustal thickness.

Our interpretation of the final inversion model in
terms of crustal thickness beneath the Imperial Valley region
is shown in Figure 2. Figure 2a is a contour plot of crustal
thickness with contour levels indicated every 1.5 km. In
Figure 2b the increment between contours is increased to 6 km
to allow for plotting and comparing the major geologic fea-
tures and geothermal areas with the model. One of the most
significant features to be noted in Figure 2 is the location
of all the geothermal areas near regions of relatively thin
crust or upwelling of high temperature mantle material. In
particular, the Salton Sea KGRA, one of the largest geother-
mal fields in the Imperial Valley, is situated over a region
of pronounced crustal thinning, of the order of 10 km. This is
consistent with the hypothesis that the Salton Sea KGRA is asso-
ciated with an active spreading center. While our model also
predicts substantial mantle upwelling under Cerro Prieto, the
location of a presumed spreading center, the lack of seismic

7
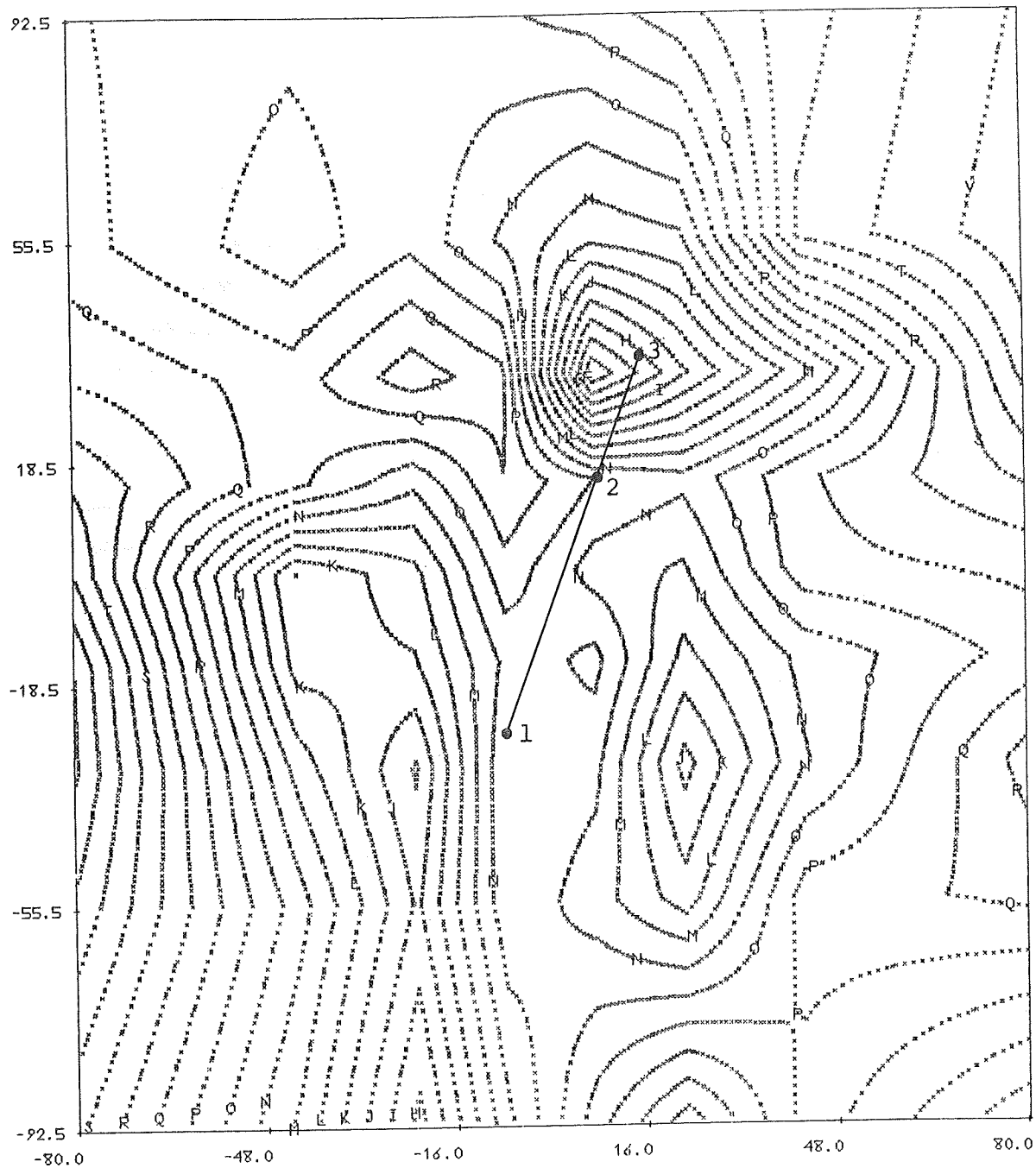
Figure 2a. Crustal thickness map obtained from final inversion model. The contour increment is 1.5 km with extreme levels of F= 7.5 km and W = 33 km. The uncertainty in the maximum and minimum crustal thickness resulting from a reasonable range of values for crust and mantle densities is given in Table 3, Section III. The straight line connecting points 1, 2 and 3 is a profile from Hill, et al., 1975b along which the maximum depths of earthquakes were observed to vary from 15 km between points 1 and 2 to about 8 km near point 3. The geographical area covered in this figure is the same as in Figure 1.

8
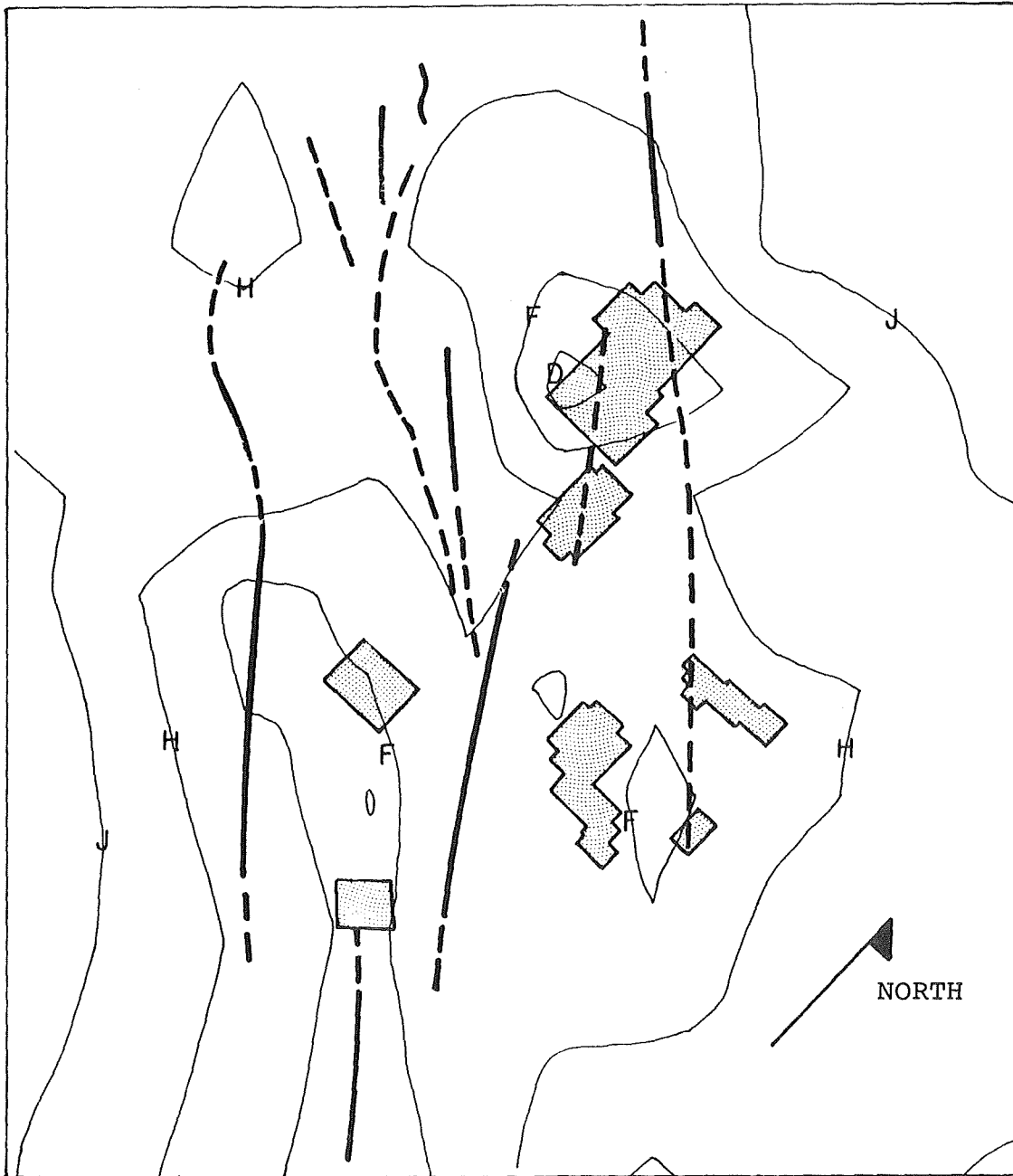
Figure 2b. Comparison of crustal thickness model with surface geologic and geothermal features.

and gravity data results in very low resolving power in this region of the model. These regions of thin crust contrast strongly with the Peninsular Ranges and Chocolate Mountain areas where the crust thickens to values in excess of 30 km.

Before continuing we must mention the uncertainty associated with assigning actual values of crustal thickness at any specific location in the model. This uncertainty arises from several possible factors ranging from an inappropriate value assumed for the crust-mantle density contrast to the occurrence of near-surface localized zones of high density sediments and/or igneous intrusions (Biehler, (1971). In light of these possibilities, the amount of crustal thinning predicted by this model under the Salton Sea KGRA is considered to be a maximum estimate. The presence of several high density rhyolite domes and the observed occurrence of cementation of sediments in this region (Elders, et al., 1972) would be mapped into the crustal thickness model as a region of exaggerated thinning. These points are treated in more detail in Section III, including quantitative estimates of their effects.

Other significant correlations that can be seen in Figure 2 are (1) the location of several of the major fault systems (e.g., the Imperial, Sand Hills and San Jacinto) over regions of large gradients in crustal thickness, and (2) the intrusion of relatively thick crust well into the valley under the Fish Creek and Superstition Mountains. It is also interesting to note that sites of relatively frequent seismic swarm activity, and no known history of major earthquakes (M $\geq$ 6.0; Richter, 1958), are located over regions of relatively thin crust, such as north of Brawley and near the southeastern edge of the Salton Sea (Hill, et al., 1975a; Hill, 1977). Swarm type activity has also been observed at the East Mesa KGRA (Combs and Hadley, 1977).

Hill, et al., 1975b reported a systematic decrease in the focal depths of earthquakes proceeding northwest along

10

the Imperial and Brawley faults between the points marked 1 and 3 in Figure 2. From 1 to 2 the maximum focal depths of earthquakes were computed to be about 15 km, while at 3 the event focal depths, at least during the time period of their study, did not exceed 7 to 8 km. While a possible systematic variation in the crustal velocity model used to locate these events might explain the variation in focal depths, the manner in which the event depths and crustal thickness correlate, in conjunction with the spatial variation in the mode of stress release in this region, suggests an alternate explanation. Namely, the relatively thin and presumably hot crust near the Salton Sea cannot support the storing of stress levels suffi- ciently large to initiate and dynamically maintain rupture conditions over fault dimensions corresponding to a large earthquake. On the other hand, along the Imperial fault where the crust is predicted to be thicker and correspondingly cooler, large earthquakes can and do occur.

The crustal thickness model in Figure 2, defined over the 72 cell centers of the model, was fit with a quadratic surface. This resulted in a regular grid of more than 4000 points with a spacing of 2.5 km. These points were plotted with different perspectives in three-dimensional hidden line form. Figure 3a is a three-dimensional plot of upper mantle topography beneath the Imperial Valley. The observer is looking down at the valley from a platform 600 km high over a point in the Pacific Ocean approximately 1000 km due south of the center of the model. The model center is located on the x-y plane at Z = 50 km at a point 15 km due south of Brawley. Figure 3b is a view from the north at distances from the model the same as in Figure 3a. The most notable feature on either of these figures is the substantial mantle upwelling under the Salton Sea. One can also clearly iden- tify two southeast to northwest trending regions of crustal thinning which are the approximate locations of the remaining Imperial Valley KGRA's.

SALTON SEA KGRA

EAST MESA, DUNES

W

E

S

z = 50 km
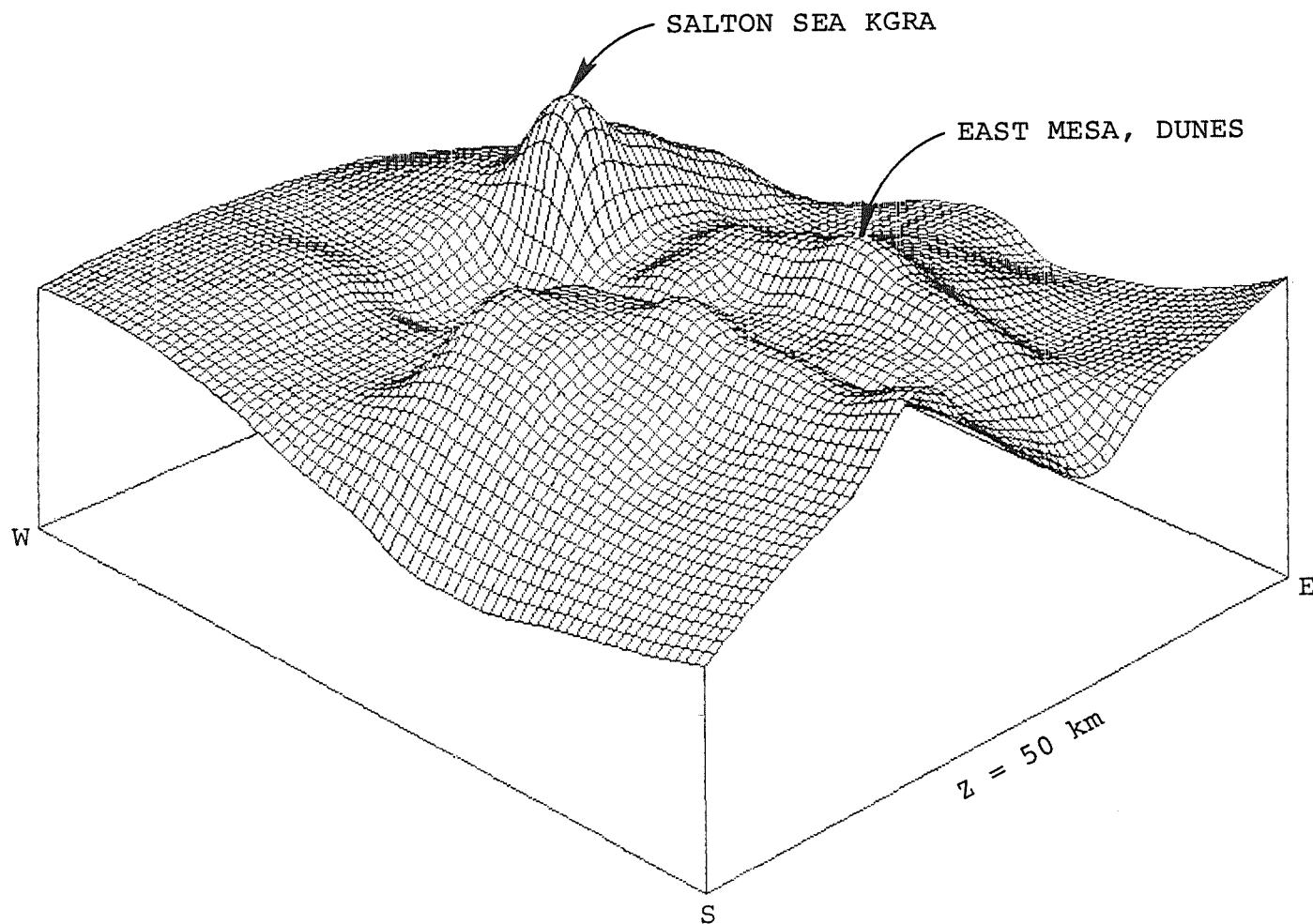
12

Figure 3a. Upper mantle topography beneath the Imperial Valley as viewed from a location over the Pacific Ocean 600 km high and 1000 km due south of the center of the model. The surface projection of the center of the model (up from a depth of 50 km) is located 15 km south of Brawley. The horizontal dimensions of the model are 160 km (N to W) and 185 km (N to E). The arrows point to the locations at depth of the KGRA's assuming these points project vertically down from their surface locations.
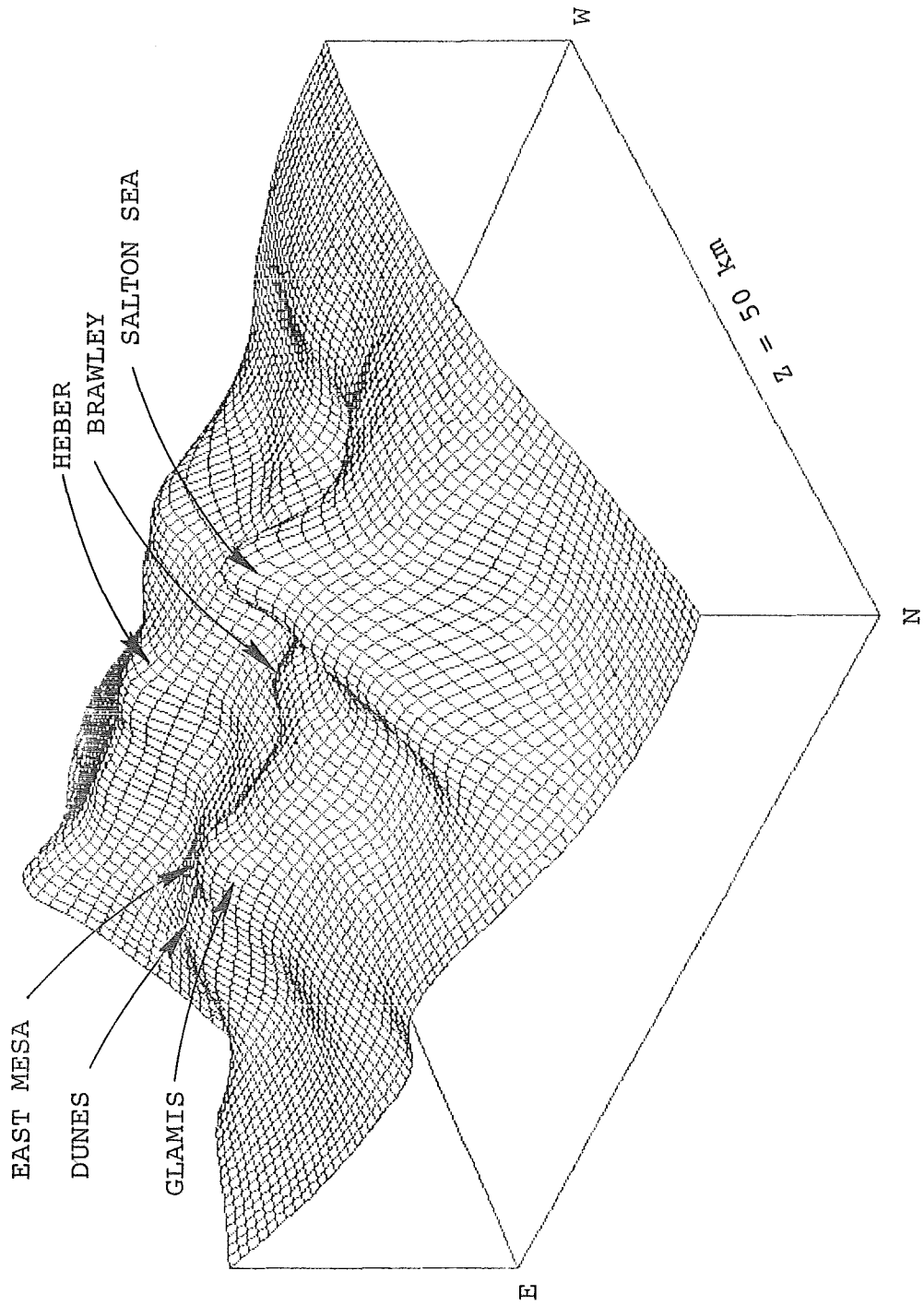
Figure 3b. Upper mantle topography beneath the Imperial Valley as viewed from the north. The observation point is 600 km high, approximately over Boise, Idaho.

The acid test for the applicability of an inversion model is how well that model predicts observed data. In Figure 4 we compare the predicted and observed gravity and travel-time data sets. Figure 4a compares the gravity data and, as can be seen, the fit is quite good. In fact, over most of the region the predicted and observed data agree to within 4 milligals as compared to a total observed anomaly of 60 milligals. In the case of the travel-time data (Figure 4b) the inversion model accounts for most of the observed anomalies, both in magnitude and azimuthal dependence. The scatter inherent in these travel-time data, however, precludes the possibility of obtaining a fit to the details of the azimuthal variation.

1.5   THE METHOD AS AN EXPLORATION TOOL

The results obtained from this numerical modeling experiment point up the effectiveness of a simultaneous inversion of different geophysical data sets for deducing earth structure. A formal inversion yields an optimal numerical model of the subsurface and a description of its uniqueness, which in turn provides a measure of the resolving power of the inverted data. An important conclusion from the Imperial Valley study was that the resolving power of a combined gravity/travel-time data set exceeds their individual resolving power. Inverted separately, travel-times from near vertical ray paths and gravity data are somewhat ambiguous in determining the depth of an anomaly. In a joint inversion, however, gravity and travel-times complement each other and remove much of this ambiguity because their sensitivity to depth variations is different.

It should be noted that the full potential of this modeling procedure was not realized in this study because of the less than optimal spatial configuration and teleseismic event recording capabilities of the Imperial Valley array.
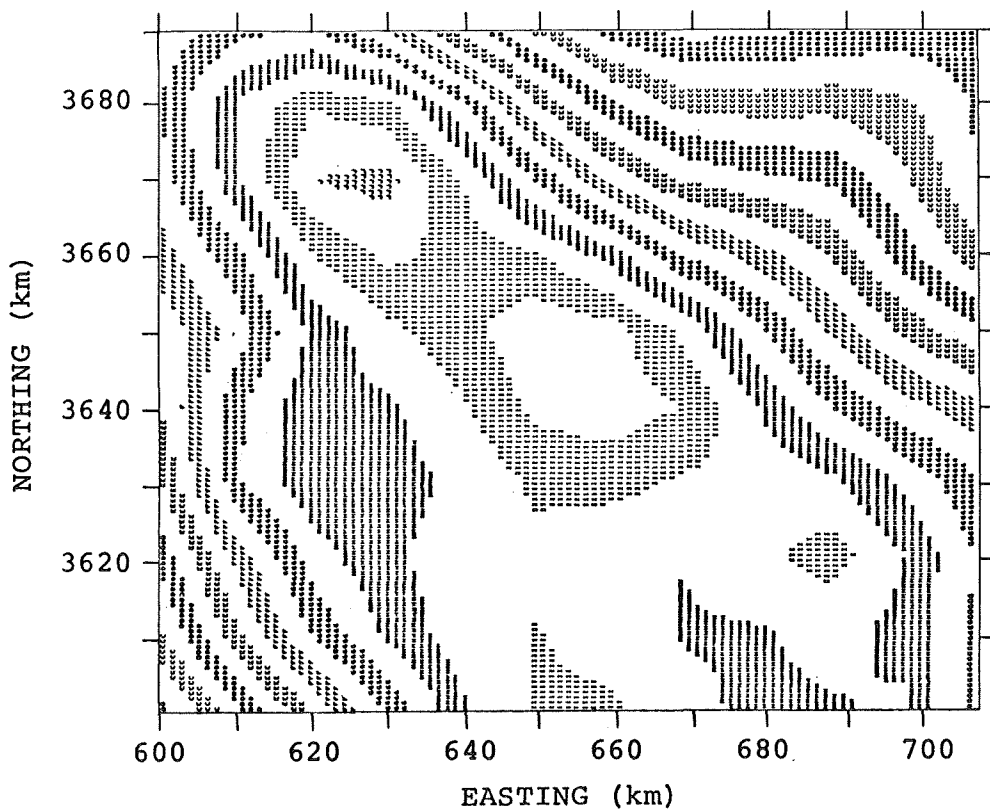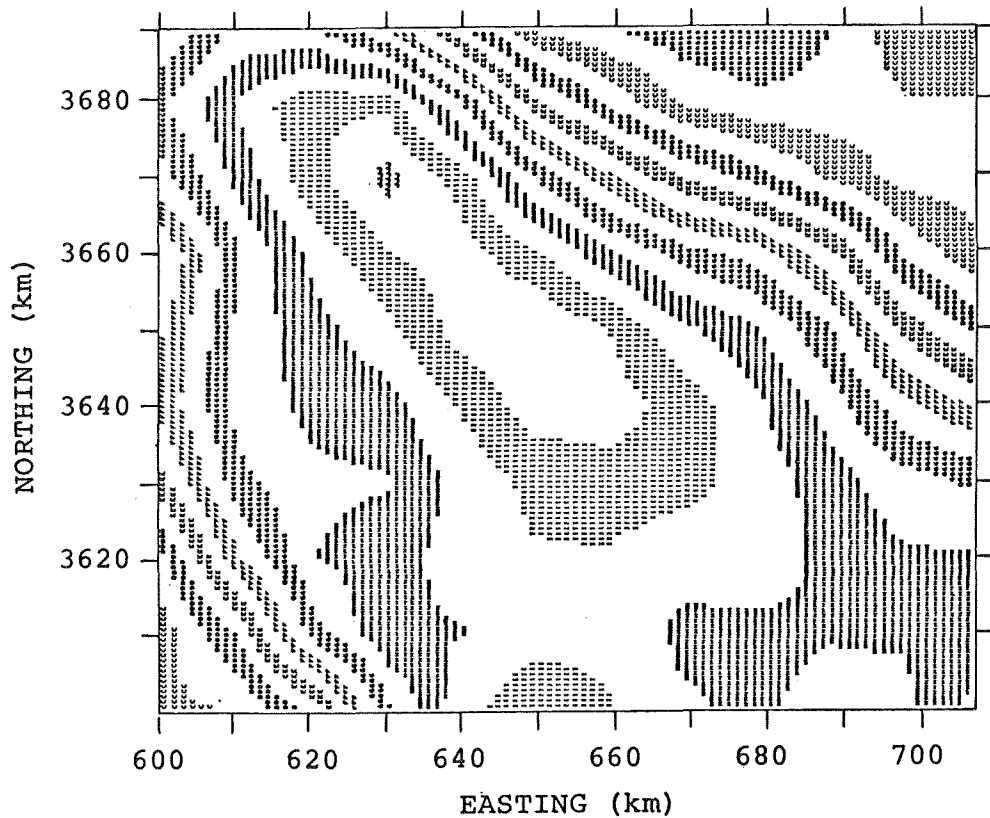
Figure 4a.   Comparison of observed gravity data (top) and
             gravity data predicted by final inversion model
             (bottom).   Each band of symbols or blank area
             defines a 4 milligal range.   C denotes -48 to
             -44 milligals.   J denotes 8 to 12 milligals.
             The areal coverage of these data with respect
             to inversion cell-model shown in Figure 4c.

15
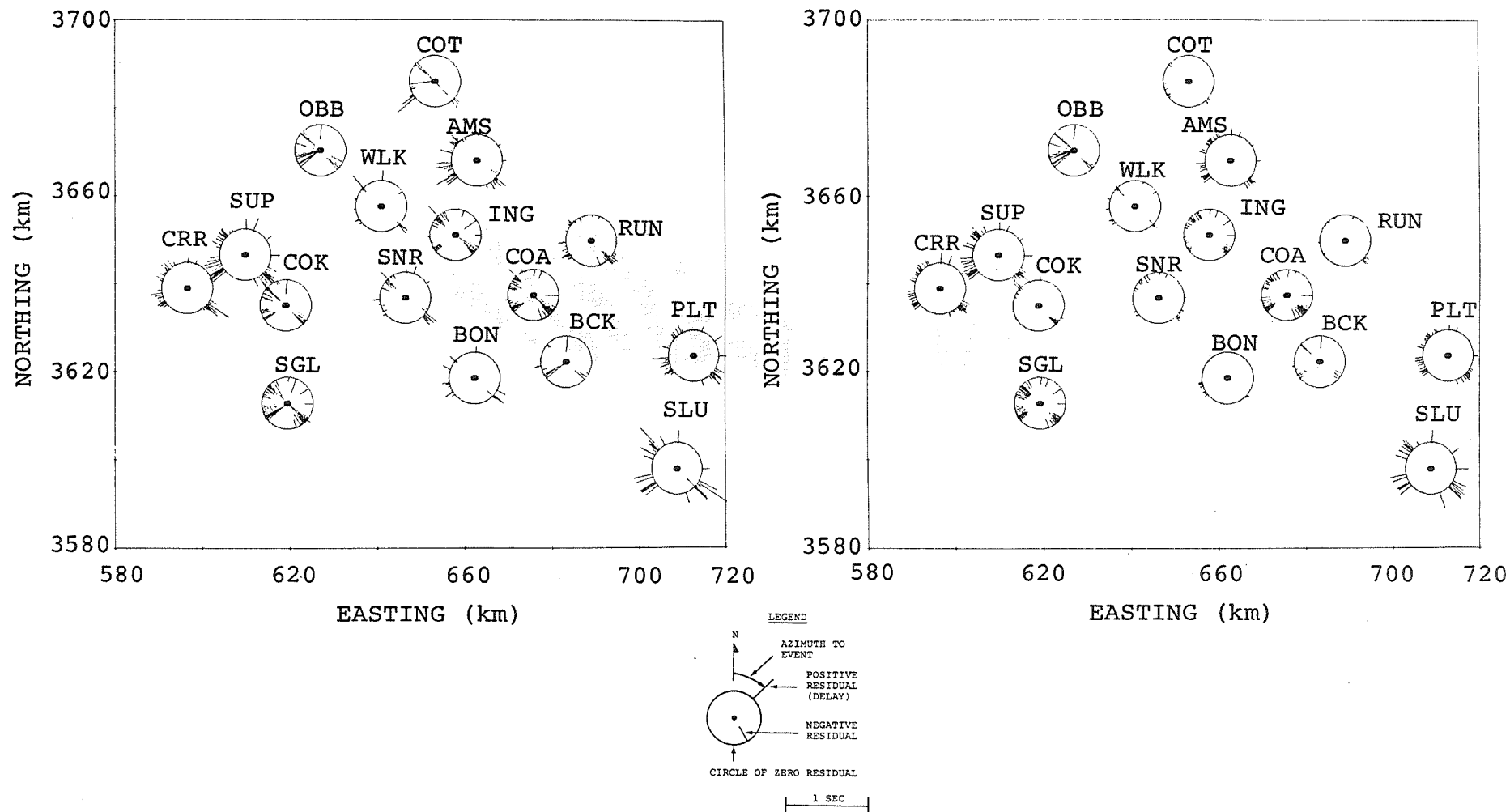
Figure 4b. Comparison of observed relative travel-time residuals (left) and residuals predicted by the final inversion model (right). Each of the small solid circles represents the location of a seismic station. Residuals are plotted at each event-station azimuth as lines radiating outward (residuals > 0) or inward (residuals < 0) from circumference of circles (see legend).

16
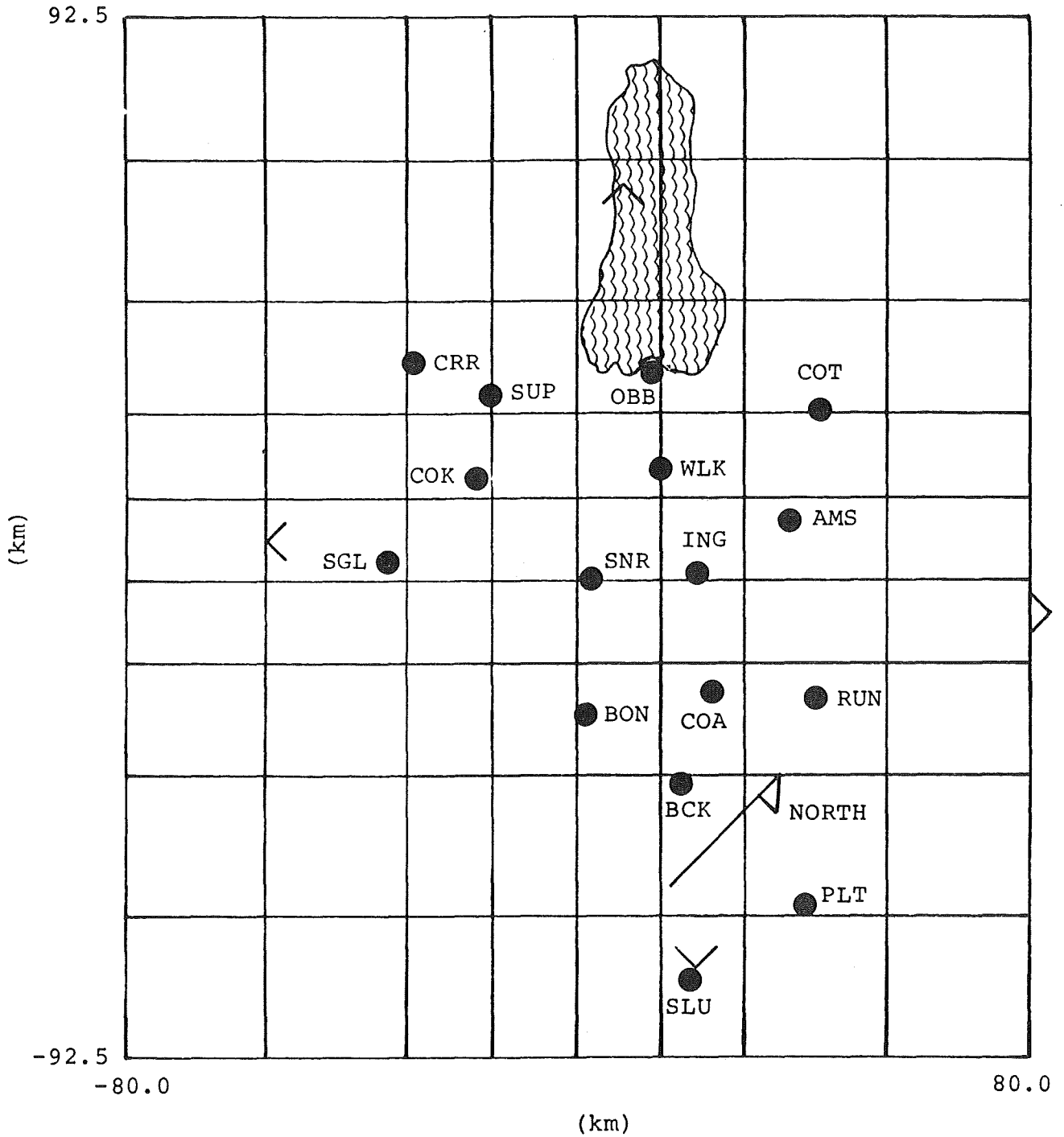
Figure 4c. Locations of seismic stations and corners of gravity data grid with respect to inversion cell model. Area covered by this figure same as in Figures 1, 2 and 3.

17

More optimal seismic arrays, in terms of station spacing and signal-to-noise ratios for teleseismic events, have been, or are being, operated in other geothermal regions (e.g., Coso Hot Springs, Yellowstone) and we strongly recommend the application of the modeling techniques developed under this program to these regions.

The incorporation of additional geophysical data sets is the next logical step in the further development of the modeling technique. For example, a substantial increase in resolving power could be realized by the addition of local earthquake data. This would provide signals with shorter wavelengths and shallower angles of incidence than teleseismic signals, thus providing additional independent information about the subsurface velocity structure. The full power of the method will be realized with the development of a capability for inverting multiple data sets such as gravity, travel-time, surface wave, electromagnetic and heat flow. This would provide a completely integrated interpretation of the earth's near-surface structure.

II. TECHNICAL DISCUSSION

2.1 STATEMENT OF THE PROBLEM

As applied in geophysics, inversion is a method for inferring the earth's physical structure from a set of experimental data. The primary aim of inversion is to derive an optimal model of the subsurface - a model that is consistent with all available geophysical data and that conforms to our prior geophysical and geological ideas of what the subsurface is like. In a "joint" or "combined" inversion, data from one or more geophysical surveys are interpreted simultaneously and systematically in terms of both an optimal model and a description of its uniqueness. In the Imperial Valley study, a combined set of gravity and teleseismic P-wave travel-time data were inverted to infer the density and compressional velocity in the upper 33 km beneath the valley. This chapter describes the techniques used to solve this inverse problem.

A set of experimental data and a set of parameters that describe a model of the earth can be denoted by the vectors $\underline{d}$ and $\underline{p}$, respectively, and in general are related by

$$\underline{d} = \underline{A}(\underline{p}) + \underline{e}, \tag{1}$$

where $\underline{A}$ is a vector of "data functionals" that describe theoretically the ideal experiment attempted in measuring $\underline{d}$, and where $\underline{e}$ is a vector of experimental errors. The evaluation of $\underline{A}$ at a model, known as "forward modeling," produces the data vector we predict would be measured in the absence of experimental error on an "earth" described by that model.

The stochastic interpretation of Equation (1) is that $\underline{d}$ is a statistical estimate for $\underline{A}(\underline{p})$ and $\underline{e}$ is the error of estimation. The "forward problem" can be described as the problem of finding $\underline{d}$ for a given model $\underline{p}$, assuming $\underline{e}$ is zero.

19

We must know how to solve this problem - namely, how to evaluate the data functionals - before the inverse problem can be solved. In the "inverse problem" $\underline{d}$ is given, $\underline{p}$ is unknown, and $\underline{e}$ is not zero. A solution to the inverse problem is an optimal estimate for $\underline{p}$, derived as a function of $\underline{d}$ and a description of its accuracy. This description normally takes the form of an expected value and a variance of $\underline{e}$, denoted $E(\underline{e})$ and $\mathrm{Var}(\underline{e})$, respectively.

2.2   FORWARD MODELING

The gravity and travel-time forward problems were solved for three-dimensional earth models composed of N homogeneous rectangular cells of arbitrary density and velocity. A model consists of a number of layers between the earth's surface and a finite depth Z_{max}. Each layer contains a two-dimensional grid of cells, where the cells at the outer edges can be arbitrarily large in order to simulate a model of infinite lateral extent.

A particular earth structure is uniquely defined by the X, Y and Z coordinates of the cell interfaces, an N by 1 density vector $\underline{\rho}$, and an N by 1 slowness (reciprocal velocity) vector $\underline{a}$. Each component of $\underline{\rho}$ or $\underline{a}$ is a value of density or slowness in a cell.

A three-dimensional cell-model can describe a wide variety of earth structures. Any discrete model parameterization, though, has inherent limitations on its ability to describe all possible structures. The cell-model does not describe density and slowness variations within the boundaries of a cell nor density and slowness below Z_{max}. However, these limitations were accounted for by our data processing procedure and inversion algorithm. In addition, it was found that many non-homogeneous-cell structures could be accurately modeled by "volume weighted" homogeneous cells (Savino, et al., 1977).

The gravity/travel-time inverse problem was posed with density and slowness as unknown parameters and with cell coordinates as known. The gravity and travel-time data functionals are therefore functions of density and slowness.

2.2.1 Forward Gravity Modeling

Let $\underline{g}$ be a vector whose components are the values of vertical gravity at an array of stations on the earth's surface. The vector $\underline{g}$ due to a density model $\underline{\rho}$ is given by

$$\underline{g} = G\underline{\rho} + \underline{\gamma} \tag{2}$$

(Savino, et al., 1976, 1977), where G is the "gravity kernel matrix," the ith column of which is the gravity field due to a unit density i^{th} cell. The first term in Equation (2) is the gravity field due to the earth's density between $Z = 0$ and $Z = Z_{max}$. The gravity field due to density below Z_{max}, in effect the rest of the earth, is written symbolically as $\underline{\gamma}$ and can be thought of as a regional gravity field.

In Equation (2), $\underline{g}$ represents the total gravity field that would be measured on the earth's surface. A related forward problem is to calculate the anomalous gravity field, $\delta\underline{g}$, due to an anomalous density, $\delta\underline{\rho}$, above Z_{max}. Since the relationship between $\underline{g}$ and $\underline{\rho}$ is linear, $\delta\underline{g}$ is given by

$$\delta\underline{g} = G \, \delta\underline{\rho} \quad .$$

2.2.2 Forward Travel-Time Modeling

The teleseismic travel-time forward problem is to calculate the travel-time residuals from an event of known location

21

to an array of stations through a given velocity model. A
residual travel-time is a travel-time minus the predicted
Herrin travel-time for the known event-station distance.

Fermat's principle implies that the travel-time from
Event e to Station s through slowness distribution a is
given to first order by (see Figure 5)

$$t_{es} = \int_e^{s'} d\xi \ a(\xi) + \int_{s'}^{s} d\xi \ a(\xi), \tag{3}$$

where ξ is distance along the path of integration, which is
the geometrical ray path through a radially symmetric refer-
ence velocity model. This reference path has the Herrin model
(a_H) ray parameter for the event-station distance. Therefore,
the path segment ss′ is found by ray-tracing downward from
the station with the given ray parameter.

The travel-time from e to s predicted by the Herrin
model, t_{es}^H, is obtained by substituting a_H for a in Equation
(3). Therefore, the travel-time residual at Station s can
be written

$$t_{es}^R = t_{es} - t_{es}^H = \int_{s'}^{s} d\xi \ a(\xi) - \int_{s'}^{s} d\xi \ a_H(\xi)$$

$$\tag{4}$$

$$+ \int_e^{s'} d\xi \ [a(\xi) - a_H(\xi)].$$

In vector notation, t_{es}^R, t_{es}, and t_{es}^H are components of vectors
$\underline{t}_e^R$, $\underline{t}_e$, and $\underline{t}_e^H$, respectively, whose lengths are S_e, the number
of stations that record Event e. The relationship of $\underline{t}_e^R$ to a
slowness cell-model $\underline{a}$ is

$$\underline{t}_e^R = T_e \ \underline{a} + \underline{\tau}_e, \tag{5}$$
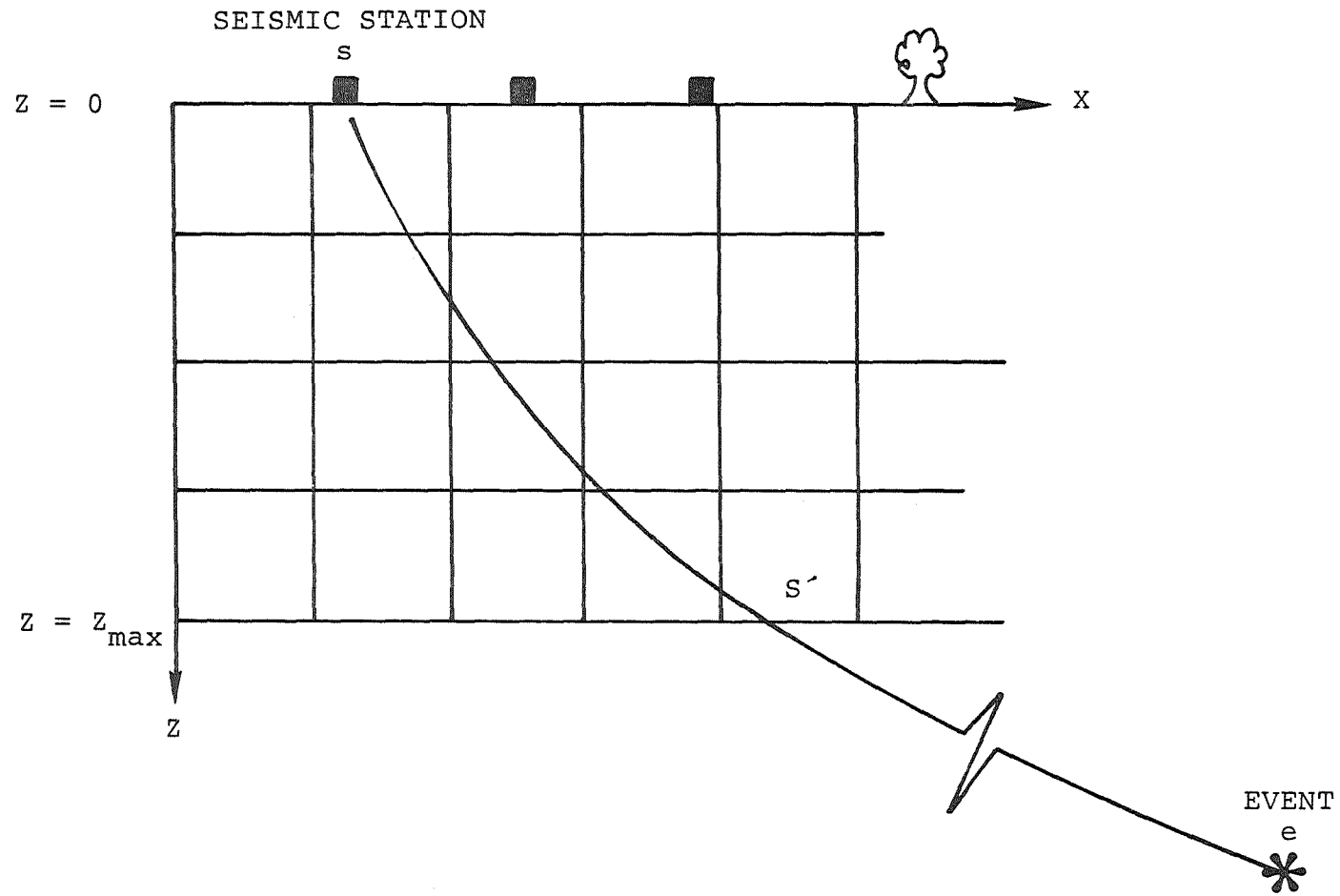
Figure 5. Ray path (ess´) from an event (e) to a seismic station (s) through reference velocity model.

where T_e is the "travel-time kernel matrix," whose components are reference path lengths through the model cells. The sth component of $\underline{\tau}_e$ is the sum of the second and third terms in Equation (4). From Equation (5), we see that the anomalous residuals due to an anomalous slowness, $\delta\underline{a}$, above Z_{max} are given by

$$\delta\underline{t}_e^R = T_e\ \delta\underline{a}\ .$$

2.3   DATA PROCESSING

Comparing Equations (2) and (5) to (1), we see that the equations that relate observed travel-time residuals for E events and observed gravity data to a density-slowness model are

$$\underline{g} = G\underline{\rho} + \underline{\Upsilon} + \underline{\varepsilon}_g \tag{6}$$

$$\underline{t}_e^R = T_e\ \underline{a} + \underline{\tau}_e + \underline{\varepsilon}_e\ ,\ e = 1,\ \ldots,\ E, \tag{7}$$

where $\underline{\varepsilon}_g$ and $\underline{\varepsilon}_e$ are the error vectors in the gravity data and travel-time residuals for Event e, respectively. To facilitate an inversion algorithm, we assume that the components of $\underline{\varepsilon}_g$ and $\underline{\varepsilon}_e$ are zero-mean and uncorrelated. Specifically,

$$E(\underline{\varepsilon}_g) = 0,\ Var\ (\underline{\varepsilon}_g) = \textstyle\sum_g^2\ , \tag{8}$$

$$E(\underline{\varepsilon}_e) = 0,\ Var\ (\underline{\varepsilon}_e) = \textstyle\sum_e^2,\ e = 1,\ \ldots,\ E, \tag{9}$$

where Σ_g and Σ_e are diagonal matrices containing the standard deviations of the gravity data and residuals from Event e, respectively.

This section describes the processing procedures that are required to produce data which obey Equations (6) through (9) and to derive estimates of their standard deviations.

2.3.1 Gravity Data Processing

The gravity data for the Imperial Valley study consisted of about 14,000 Bouguer and terrain corrected observations provided by Professor Shawn Biehler of the University of California at Riverside. To facilitate the processing and inversion of these data, they were converted to a regular rectangular grid of 644 values, spaced 4.88 km apart, by a least-squares quadratic surface interpolation technique. The technique is described by Savino, et al., (1977). We denote the resulting grid of gravity data by the vector $\underline{g}'$, which is related to $\underline{\rho}$ by

$$\underline{g}' = G'\underline{\rho} + \underline{\gamma}' + \underline{\varepsilon}_g' . \tag{10}$$

The vector $\underline{\gamma}'$ is the regional gravity field. Its role in the formulation of the inverse problem is discussed in the next section. The error vector $\underline{\varepsilon}_g'$ represents all the contributions to $\underline{g}'$ other than the regional field and the gravity field due to the density structure $\underline{\rho}$. These contributions include

1. Reading errors.

2. Bouguer correction and interpolation errors.

3. Gravity effects of the earth's density variations between model cell boundaries.

The largest source of error is expected to be the third. It was reduced and uncorrelated with two procedures. The first was a correction for the anomalous gravity field due to the

low-density sedimentary section in the upper 6 km of the crust. The second procedure was to low-pass filter and decimate the corrected gravity field.

The sediment correction was calculated by forward modeling the upper 6 km with a finely gridded cell model, or "small-grid" model. The resulting gravity small-grid correction is given by

$$\delta \underline{g}^{SG} = G^{SG} \, \delta \underline{\rho}^{SG}$$

where G^{SG} is the gravity kernel matrix for the small-grid model and $\delta \underline{\rho}^{SG}$ is the vector of sediment-minus-basement density contrasts for the model, all of which were negative. The small-grid model was derived from depth-to-basement maps for the Imperial Valley. It and the small-grid correction are presented in Section III.

The purpose of low-pass filtering the small-grid corrected data is to suppress the short-wavelength components caused by possible near-surface small-scale density variations. However, a low-pass filter also correlates the errors of gravity values at neighboring grid points. Decimating the filtered data to a courser grid produces a final data vector with reduced correlations. Decimation also removes some of the redundancy in the data.

The relationship between the primed and unprimed quantities of Equations (6) and (10) are

$$\underline{g} = F_L \, (\underline{g}' - \delta \underline{g}^{SG})$$
$$G = F_L \, G'$$
$$\underline{\gamma} = F_L \, \underline{\gamma}'$$
$$\underline{\varepsilon}_g = F_L \, (\underline{\varepsilon}_g' - \delta \underline{g}^{SG}) \tag{11}$$

26

where $\underline{g}$ is the final gravity data vector and F_L is the low-pass/decimate filter. It is not necessary to filter G', the gravity kernel matrix for $\underline{g}'$, in order to obtain G, the kernel matrix for $\underline{g}$. If the filter F_L is designed properly and does not remove gravity effects attributable to $\underline{\rho}$, decimating the appropriate rows of G' suffices. Similarly, since the regional gravity field is a slowly varying function of position, it is unaffected by a low-pass filter. Hence $\underline{\gamma}$ is simply a decimated version of $\underline{\gamma}'$.

The error vector, $\underline{\varepsilon}_g$, for the final gravity data has the same three contributions as $\underline{\varepsilon}_g'$, only filtered, decimated, and corrected for the sedimentary section. An additional source of error, probably the largest, is the errors in the small-grid correction caused by the use of an approximate model of the sediments. We estimated this error to be of the order of 3 milligals for each of the final 219 gravity data. Therefore, the diagonal components of Σ_g were set to three.

2.3.2 Travel-Time Data Processing

Travel-time residuals were derived from recordings of 182 worldwide events at the 16 stations of the Imperial Valley array. Every station did not produce a usable record of every event so the final data base consisted of 1266 event-station seismograms. From these, 527 residuals were obtained for stations and 50 groups of events having distinct ray paths.

An accurate measure of the travel-time from an event to a given station requires an accurate estimate of the origin time of the event and a reliable determination of the first P-wave motion on the seismogram. In practice, first motion is often poorly defined because of the interference of noise with the P-waveform. Other points on the waveform, in particular the first few peaks, troughs, and zero-crossings, are more clearly identifiable. For a given event, the difference in

27

arrival time of a common clearly-defined point on the wave-
forms recorded at two stations is an accurate measure of
the difference in travel-time to the two stations and is
unaffected by uncertainties in event origin time or first-
motion determination. Therefore, differences between travel-
time residuals at different stations, or "relative residuals,"
were used in this study rather than "absolute residuals."

The residuals used in the inversion were "average-
station relative residuals," defined as absolute residuals
minus a weighted average of the absolute residuals. The
residuals determined directly from the data, however, were
"key-station relative residuals," which are absolute residuals
minus the absolute residual for a key, or reference, station.
Average-station relative residuals are obtained from either
absolute or key-station relative residuals by zero-meaning.
This part of the travel-time data processing is discussed in
the next section.

To obtain estimates for key-station relative residuals,
the arrival times of as many as nine peaks, troughs, or zero-
crossings were measured from each seismogram (Savino, et al.,
1977). Denoting the arrival time of a given pick p at Station
s for Event e by t'_{esp}, the corresponding relative residual
with respect to a reference Station r is

$$\Delta t'_{esp} = t'_{esp} - t'_{erp} - t^H_{es} + t^H_{er} , \qquad (12)$$

where the last two terms are the predicted Herrin times from
e to s and r, respectively. The relative residual for Station
s is estimated by the sample mean of the discernible picks
common to s and r:

$$\Delta t'_{es} = \frac{1}{P_{es}} \sum_{p=1}^{P_{es}} \Delta t'_{esp}, \qquad (13)$$

where P_{es} is the number of picks.

The estimate $\Delta t'_{es}$ has two primary sources of error. The first is due to delays caused by slowness variations not modeled by the cell-model slowness vector $\underline{a}$. The major error of this type is due to the sedimentary section in the upper 6 km beneath the Imperial Valley and, as with the gravity data, is compensated for by a small-grid correction. Denoting the small-grid sediment-minus-basement slowness vector by $\delta\underline{a}^{SG}$, the delays due to the sediments for Event e are given by

$$\underline{\delta t}_e^{R\,SG} = T_e^{SG}\ \underline{\delta a}^{SG}$$

where T_e^{SG} is the small-grid travel-time kernel matrix. The corrected relative residuals are

$$\Delta t_{es} = \Delta t'_{es} - \delta t_{es}^{R\,SG} + \delta t_{er}^{R\,SG}\ ,$$

where the last two terms, respectively, are the small-grid delays for Stations s and r.

The second source of error is due to reading errors and seismogram noise. Denoting the error in the arrival time t'_{esp} by ε'_{esp}, we see from Equations (12) and (13) that the corresponding error in $\Delta t'_{es}$ is

$$\Delta\varepsilon'_{es} = \frac{1}{P_{es}} \sum_{p=1}^{P_{es}} (\varepsilon'_{esp} - \varepsilon'_{erp})\ .$$

To determine the variance of $\Delta\varepsilon'_{es}$, we assume that the error in the picks for a given event are zero-mean, independent, and have a common variance σ_e^2. This implies

$$E(\Delta \varepsilon'_{es}) = 0 , \qquad\qquad\qquad\qquad (14)$$

$$\text{Cov}(\Delta \varepsilon'_{es}, \Delta \varepsilon'_{es'}) = \frac{\sigma_e^2 \, P_{ess'}}{P_{es} \, P_{es'}} (1 + \delta_{ss'} - \delta_{sr} - \delta_{s'r}) ,$$

where $P_{ess'}$ is the number of picks common to Stations s and s' and where δ is the Kronecker matrix.

From Equation (14) it is apparent that the errors in the relative residuals at different stations are correlated since their covariance is non-zero. In fact, $\Delta \varepsilon'_{es}$ can be defined as the difference between ε'_{es} and ε'_{er} where

$$\varepsilon'_{es} = \frac{1}{P_{es}} \sum_{p=1}^{P_{es}} \varepsilon'_{esp} .$$

Then Equation (14) is nearly equivalent to the assumption that

$$E(\varepsilon'_{es}) = 0 ,$$

$$\text{Var}(\varepsilon'_{es}) = \frac{\sigma_e^2}{P_{es}} , \quad \text{Cov}(\varepsilon'_{es}, \varepsilon'_{es'}) = 0 . \qquad (15)$$

ε'_{es} can be thought of as the zero-mean component of error in an estimate for the absolute residual at Station s. Of course, an estimate for the absolute residual would also have a baseline error due to the fact that the absolute travel-time to the reference station (or any station) is known much less precisely than the travel-time differences between stations.

In light of the facts that ε'_{es} is uncorrelated with $\varepsilon'_{es'}$, where s and s' are any two stations, and that the zero-meaning procedure described in the next section eliminates baseline errors, it is convenient to define an estimate for the absolute residual at s in terms of the key-station relative residual:

$$t_{es}^R = \Delta t_{es} + t_{er} - t_{er}^H ,$$

where t_{er} is an estimate for the absolute travel-time to r whose error, ε_{er}', has variance σ_e^2/P_{er}. The relationship between t_{es}^R and the slowness model $\underline{a}$ is then Equation (7) – namely

$$\underline{t}_e^R = T_e \underline{a} + \underline{\tau}_e + \underline{\varepsilon}_e ,$$

where each component of $\underline{\tau}_e$ now includes the baseline error in t_{er}. The sth components of $\underline{\varepsilon}_e$ is the sum of ε_{es}' and the error in the small-grid correction at Station s. We assume this latter error is independent of ε_{es}' and has variance σ_1^2. Referring to Equations (15) and (9), we therefore set the sth component of the diagonal variance matrix Σ_e^2 to

$$\Sigma_{es}^2 = \sigma_e^2/P_{es} + \sigma_1^2 .$$

σ_1 was taken to be 0.03 s.

The variance σ_e^2 was calculated in terms of a sample variance derived from all the picks for a given event and modified to ensure that it did fall below some minimum σ_2^2:

$$\sigma_e^2 = \sigma_2^2 + \left[\sum_{\substack{s=1 \\ s \neq r}}^{S_e} (P_{es} - 1) \right]^{-1} \sum_{s=1}^{S_e} \sum_{p=1}^{P_{es}} (\Delta t_{esp}' - \Delta t_{es}')^2$$

For σ_2 we again used 0.03 s.

The final step of data processing consisted of averaging together the residuals for events very close in location whose ray paths to a given station were nearly coincident. These group averages were treated as individual events. The group residuals and variances were computed as

$$\Delta t_{gs} = \sum_{e=1}^{E_g} P_{es} \, \sigma_e^{-2} \, \Delta t_{es} \bigg/ \sum_{e=1}^{E_g} P_{es} \, \sigma_e^{-2} \; ,$$

$$\sigma_g^2 = 1 \bigg/ \sum_{e=1}^{E_g} P_{es} \, \sigma_e^{-2} \; ,$$

where g denotes a group of E_g events.

2.4   FORMULATION OF GRAVITY/TRAVEL-TIME INVERSION

The processed gravity data, $\underline{g}$, and travel-time residuals, $\underline{t}_e^R$, $e = 1, \ldots, E$, are related to $\underline{\rho}$ and $\underline{a}$ by Equations (6) through (9). In this section we combine Equations (6) and (7) into a single relationship of the form Equation (1), to which our inversion algorithm can be applied.

2.4.1 Gravity Inverse Problem

Recall from Equations (6) and (8) that the relationship between $\underline{g}$ and $\underline{\rho}$ was

$$\underline{g} = G\underline{\rho} + \underline{\gamma} + \underline{\varepsilon}_g \; , \tag{6}$$

$$E(\underline{\varepsilon}_g) = 0 \; , \quad \text{Var}(\underline{\varepsilon}_g) = \Sigma_g^2 \; , \tag{8}$$

where Σ_g is a diagonal matrix of standard deviations of the components of the error vector $\underline{\varepsilon}_g$.

Comparing Equation (6) to Equation (1), we see that the role of the gravity field $\underline{\gamma}$ may be interpreted two ways. First, we could treat $\underline{\gamma}$ as an additional unknown parameter vector and solve for it together with $\underline{\rho}$. Second, we could treat it as an

32

error term like $\underline{\varepsilon}_g$ and specify its mean and variance. These two approaches are equivalent for a given assumption about the form of $\underline{\gamma}$. We adopt the second approach since $\underline{\gamma}$ is not an unknown of interest as is $\underline{\rho}$.

The mean of $\underline{\gamma}$ corresponds to a possible known component in the regional gravity field - namely, a known baseline or the gravity field due to a known density anomaly below Z_{max}. The variance of $\underline{\gamma}$ expresses the expected size and form of unknown gravity effects from below Z_{max}. This variance matrix must have large covariances since a regional field is slowly varying and thus correlated between gravity stations. While our inversion algorithm can handle nondiagonal variance matrices with no conceptual difficulty, it is more meaningful to transform Equation (6) into an equivalent equation in which the error term has zero-mean and a diagonal variance. The appropriate transformation produces a data vector $\Delta\underline{g}$ given by

$$\Delta\underline{g} = F_g(\underline{g} - E \underline{\gamma})$$

where the matrix F_g is

$$F_g = \sum_g [\text{Var} (\underline{\varepsilon}_g + \underline{\gamma})]^{-1/2}. \tag{16}$$

$( )^{-1/2}$ denotes the inverse of the square root of a matrix. This transformation is a deregionalization operator - the subtraction of the mean of $\underline{\gamma}$ corrects for a known regional field and multiplication by F_g filters the result. Applying the transformation to each term in Equation (6) produces

$$\Delta\underline{g} = \Delta G \underline{\rho} + \Delta\underline{\varepsilon}_g \quad ,$$

$$E(\Delta\underline{\varepsilon}_g) = 0, \quad \text{Var} (\Delta\underline{\varepsilon}_g) = \sum_g^2 \quad , \tag{17}$$

where

$$\Delta \underline{g} = F_g \ (\underline{g} - E \ \underline{\gamma})$$

$$\Delta G = F_g \ G$$

$$\Delta \underline{\varepsilon}_g = F_g \ (\underline{\varepsilon}_g + \underline{\gamma} - E \ \underline{\gamma}) \tag{18}$$

If the variance assumed for $\underline{\gamma}$ is complicated, the computation of F_g may be very difficult. Therefore, we assume the regional field is at worst a linear trend of the form

$$\underline{\gamma} = \gamma_1 \ \underline{1} + \gamma_x \ \underline{x} + \gamma_y \ \underline{y} \quad , \tag{19}$$

where γ_1, γ_x, and γ_y are scalars, $\underline{1}$ is a vector all of whose components are one, and $\underline{x}$ and $\underline{y}$, respectively, are vectors containing the x and y coordinates of the gravity stations. The mean and variance of $\underline{\gamma}$ is expressed in terms of the means and variances of γ_1, γ_x, and γ_y.

Equations (19) and (16) imply that the filter F_g is a detrending operator of the form

$$F_g = I - \alpha_1 \ \underline{1} \ \underline{1}^T \ \textstyle\sum_g^{-2} - \alpha_x \ \underline{x} \ \underline{x}^T \ \textstyle\sum_g^{-2} - \alpha_y \ \underline{y} \ \underline{y}^T \ \textstyle\sum_g^{-2} \ .$$

$$\tag{20}$$

The scalars α_1, α_x, and α_y are functions of variances specified for γ_1, γ_x, and γ_y, respectively.

We assume the variance of γ_1 is very large, stating in effect that the baseline of the gravity data is unknown. Therefore, α_1 approaches the value $\underline{1}^T \ \textstyle\sum_g^{-2} \ \underline{1}$ and F_g zero-means.

34

Since the density above Z_{max}, $\underline{\rho}$, can contribute to $\underline{g}$ a slowly varying component which might have the same form assumed for the regional field, the filter F_g may remove some of the gravity effect due to $\underline{\rho}$ along with the regional field. This possibility is compensated for by the use of ΔG as the kernel matrix relating $\Delta \underline{g}$ and $\underline{\rho}$. The use of G in place of ΔG in Equation (17) would be incorrect.

2.4.2 Travel-Time Inverse Problem

We saw that the observed travel-time residuals from E events are related to $\underline{a}$ by

$$\underline{t}_e^R = T_e\underline{a} + \underline{\tau}_e + \underline{\varepsilon}_e \ , \ e = 1, \ \ldots, \ E \tag{7}$$

with

$$E(\underline{\varepsilon}_e) = 0, \ \ \text{Var} \ (\underline{\varepsilon}_e) = \sum_e^2 \ , \ e = 1, \ \ldots, \ E. \tag{9}$$

where Σ_e is the diagonal matrix of standard deviations for the residuals from Event e.

Each component τ_{es} of $\underline{\tau}_e$ is the sum of 1) the residual accumulated between Event e and Z_{max}, 2) the Herrin travel-time between $Z = 0$ and $Z = Z_{max}$, and 3) the baseline error in an estimate for the travel-time to the key station. For a given event, each of these contributions to τ_{es} can be expected to be either the same for each station or a slowly varying function of station position. Therefore, $\underline{\tau}_e$ can be treated as a "regional" contribution to the data from Event e and handled as we handled $\underline{\gamma}$ in the gravity problem, an approach similar to the one used by Aki, et al., 1977.

We assume $\underline{\tau}_e$ is at worst a linear tread:

$$\underline{\tau}_e = \tau_{e1} \ \underline{1} + \tau_{ex} \ \underline{x} + \tau_{ey} \ \underline{y} \tag{21}$$

35

It is therefore removed from the data by a transformation of
the form in Equation (20). Denoting the detrending operator
for Event e by F_e, we obtain

$$\Delta \underline{t}_e = \Delta T_e \ \underline{a} + \Delta \underline{\varepsilon}_e \ ,$$

$$E(\Delta \underline{\varepsilon}_e) = 0, \quad \text{Var} \ (\Delta \underline{\varepsilon}_e) = \sum_e^2 \ , \tag{22}$$

where

$$\Delta \underline{t}_e = F_e \left[\underline{t}_e^R - E(\underline{\tau}_e) \right]$$

$$\Delta T_e = F_e \ T_e$$

$$\Delta \underline{\varepsilon}_e = F_e \left[\underline{\varepsilon}_e + \underline{\tau}_e - E(\underline{\tau}_e) \right] \tag{23}$$

The expected value of $\underline{\tau}_e$, $E(\underline{\tau}_e)$, is effectively a correction
for a known residual, such as due to a known mantle inhomogeneity.

For the Imperial Valley, we treated $\underline{\tau}_e$ as only an unknown
baseline by assuming τ_{el} had a very large variance and τ_{ex} and
τ_{ey} had zero variances. In this case, F_e is simply a zero-
meaning operator and $\Delta \underline{t}_e$ is a vector of average-station rela-
tive residuals. As a result, $\Delta \underline{t}_e$ is unaffected by any baseline
errors or errors in event origin time and event location.

2.4.3 Joint Gravity/Travel-Time Inverse Problem

As they stand, Equations (17) and (22) are uncoupled
equations for $\underline{\rho}$ and $\underline{a}$, respectively. We couple them by
assuming a relationship between slowness and density. Any
nonlinear relationship can be approximated by a linear one
of the form

$$\rho = c_1 \, a + c_2 \, ,$$

for geologically reasonable value of a and ρ. The constants c_1 and c_2 may be different for different layers in the model.

To write this relation in vector form, we partition $\underline{a}$ and $\underline{\rho}$ by layers. Define $\underline{\rho}(\ell)$ to be the vector of density values for the ℓth of L layers. Similarly define $\underline{a}(\ell)$:

$$\underline{\rho}^T = [\underline{\rho}(1)^T, \ldots, \underline{\rho}(L)^T]$$

$$\underline{a}^T = [\underline{a}(1)^T, \ldots, \underline{a}(L)^T] \, . \tag{24}$$

The density-slowness relationship we assume is

$$\underline{\rho}(\ell) = c_1(\ell) \, \underline{a}(\ell) + c_2(\ell) \, \underline{1} \, , \quad \ell = 1, \ldots, L. \tag{25}$$

In terms of layer partitions, Equations (17) and (22) can be written

$$\Delta \underline{g} = \sum_{\ell=1}^{L} \Delta G(\ell) \, \underline{\rho}(\ell) + \Delta \underline{\varepsilon}_g$$

$$\Delta \underline{t}_e = \sum_{\ell=1}^{L} \Delta T_e(\ell) \, \underline{a}(\ell) + \Delta \underline{\varepsilon}_e, \quad e = 1, \ldots, E, \tag{26}$$

where $\Delta G(\ell)$ and $\Delta T_e(\ell)$ are partitions of ΔG and ΔT_e.

Assuming that the filters F_g and F_e of Equations (18) and (23) zero-mean, each partition of ΔG has the useful property that

$$\Delta G(\ell) \; \underline{1} = 0 \; , \; \ell = 1, \; \ldots, \; L. \tag{27}$$

This is because a zero-meaned gravity field is insensitive to a layer of uniform density, which contributes only a constant to the total field. Similarly, since the ray paths to an array of stations from a teleseismic event are nearly parallel between the surface and Z_{max},

$$\Delta T_e \; (\ell) \; \underline{1} \doteq 0, \; \ell = 1, \; \ldots, \; L, \; e = 1, \; \ldots, \; E. \tag{28}$$

Equations (27) and (28) imply that $\Delta \underline{g}$ and $\Delta \underline{t}_e$ are insensitive to the baseline, or average value, of density and slowness in each layer. Consequently, they are sensitive only to lateral variations in density and slowness. Therefore, we define anomalous density and slowness vectors by

$$\Delta \underline{\rho}(\ell) = \underline{\rho}(\ell) - (\underline{1}^T W^{-1} \underline{1})^{-1} \underline{1} \; \underline{1}^T W^{-1} \; \underline{\rho}(\ell)$$

$$\Delta \underline{a}(\ell) = \underline{a}(\ell) - (\underline{1}^T W^{-1} \underline{1})^{-1} \underline{1} \; \underline{1}^T W^{-1} \; \underline{a}(\ell), \tag{29}$$

where W is any positive definite weighting matrix. The second terms in Equation (29) are essentially weighted averages of density and slowness in layer ℓ, respectively. Substituting Equation (29) into Equations (25) and (26) gives

$$\Delta \underline{g} = \sum_{\ell=1}^{L} c_1(\ell) \; \Delta G(\ell) \; \Delta \underline{a}(\ell) + \Delta \underline{\varepsilon}_g$$

$$\Delta \underline{t}_e = \sum_{\ell=1}^{L} \Delta T_e(\ell) \; \Delta \underline{a}(\ell) + \Delta \underline{\varepsilon}_e \tag{30}$$

and

$$\Delta \underline{\rho}(\ell) = c_1(\ell) \, \Delta \underline{a}(\ell), \quad \ell = 1, \ldots, L. \tag{31}$$

The constants $c_2(\ell)$ drop out of the problem and are only needed if we wish to relate the baselines of density and slowness in each layer.

Since Equation (30) is linear, a linear inversion technique can be used to find an estimate, $\hat{\Delta \underline{a}}(\ell)$, for $\Delta \underline{a}(\ell)$, $\ell = 1$, $\ldots$, L. Equation (31) implies that an estimate for $\Delta \underline{\rho}$ is obtained as

$$\hat{\Delta \underline{\rho}}(\ell) = c_1(\ell) \, \hat{\Delta \underline{a}}(\ell), \quad \ell = 1, \ldots, L. \tag{32}$$

The joint gravity/travel-time inverse equations in Equation (30) can be summarized by the single vector equation

$$\underline{d} = A \, \underline{P} + \underline{e}$$

$$E(\underline{e}) = 0, \text{ Var }(\underline{e}) = I \, , \tag{33}$$

where I is the unit matrix. In Equation (33), the data have been normalized by their standard deviations in order to simplify the formalism of linear inversion methods.

2.5   INVERSION METHOD

In the gravity/travel-time inverse problem, the relationship between the data vector $\underline{d}$ and parameter vector $\underline{p}$ is linear. Consequently, a linear inversion technique can be used to find an optimal estimate for $\underline{p}$. With linear inversion, an optimal estimate of the form

$$\hat{\underline{p}} = A^+ \underline{d} \qquad\qquad (34)$$

is found, where A^+ is a generalized inverse of the matrix A. In this section, we describe the techniques used to find $\hat{\underline{p}}$.

2.5.1 Optimality Criterion

Our criterion for defining an optimal estimate for $\underline{p}$ is a double one. The first criterion is that $\hat{\underline{p}}$ give a close fit to the data. Namely, $\hat{\underline{p}}$ should make $\phi_1 (\hat{\underline{p}})$ small, where

$$\phi_1 (\hat{\underline{p}}) = |\underline{d} - A\hat{\underline{p}}|^2 \equiv (\underline{d} - A\hat{\underline{p}})^T (\underline{d} - A\hat{\underline{p}}) \ .$$

$\phi_1(\hat{\underline{p}})$ is the sum of the squares of the residuals of fit between the data vector $\underline{d}$ and the data predicted by $\hat{\underline{p}}$, $A\hat{\underline{p}}$. Since $\underline{d}$ was normalized to have unit variance, no weighting coefficients are needed in the definition of ϕ_1.

The second criterion for optimality is that $\hat{\underline{p}}$ be as "smooth" as possible in some sense. Two interpretations of a smoothness criterion are 1) that $\hat{\underline{p}}$ be as small as possible and 2) that $\hat{\underline{p}}$ have the smallest spatial variations possible. Both these and other interpretations of smoothness can be expressed as the requirement that, for an appropriate matrix B, $\phi_2 (\hat{\underline{p}})$ be a minimum, where

$$\phi_2 (\hat{\underline{p}}) = |B\hat{\underline{p}}|^2 \equiv \hat{\underline{p}}^T B^T B \hat{\underline{p}} \ .$$

Because of its role in the smoothness criterion, we refer to B as a "smoothing" matrix but it is really a "roughing" operator since the minimization of roughness produces smoothness.

Our criterion for obtaining an optimal estimate is that $\hat{\underline{p}}$ minimize both ϕ_1, the misfit to the data, and ϕ_2, the

unsmoothness of the model. Unfortunately, though, no model makes ϕ_1 and ϕ_2 simultaneously absolutely minimum. However, an optimal compromise is achieved by minimizing $\phi(\hat{\underline{p}})$, where

$$\phi = \phi_1 + \alpha\, \phi_2 \ ,$$

for some positive value of α. For any α, the resulting model parameter estimate provides the smallest value of ϕ_1 of all models that have its value of ϕ_2, and vice versa (Backus and Gilbert, 1970; Jordan, 1973).

The "trade-off parameter" α regulates the relative importance of minimizing ϕ_1 compared to ϕ_2. The minimization of ϕ defines a family of model estimates, $\hat{\underline{p}}(\alpha)$, each giving its own compromise between fit and smoothness. ϕ_1 and ϕ_2 are monotone increasing and decreasing functions of α, respectively. Although every value of α produces an optimal estimate for $\underline{p}$, it is desirable to avoid values that are too large or too small and thus overly sacrifice either fit or smoothness.

For a given α, the vector $\hat{\underline{p}}$ that minimizes ϕ is

$$\hat{\underline{p}} = (A^T A + \alpha\, B^T B)^{-1} A^T \underline{d} \equiv A^+ \underline{d} \ . \tag{35}$$

The actual computation of $\hat{\underline{p}}$, however, is done with singular value decomposition as described in Section 2.5.4.

The smoothing matrix B allows us to restrict the possible solutions for $\underline{p}$ to ones that are reasonable geologically. Geologic information can also be incorporated into $\hat{\underline{p}}$ more directly by defining $\hat{\underline{p}}$ to be a perturbation to a starting model $\underline{p}_s$. In this case, $\hat{\underline{p}}$ becomes

$$\hat{\underline{p}} = \underline{p}_s + A^+ (\underline{d} - A\underline{p}_s) \ . \tag{36}$$

41

2.5.2 Smoothing Matrix

The smoothness criterion we used penalized lateral spatial variations in density and slowness with wavelengths less than a specified wavelength W. The continuous analog of the function ϕ_2 is

$$\phi_2(\hat{p}) = \int_0^{Z_{max}} dz \int_{-\infty}^{\infty} dx \int_{-\infty}^{\infty} dy \left[\hat{p}(x,y,z)^2 \right.$$

$$\left. + W^2 \left(\frac{\partial \hat{p}}{\partial x}\right)^2 + W^2 \left(\frac{\partial \hat{p}}{\partial y}\right)^2 \right] .$$

We set W to 50 km. The matrix B is defined in terms of finite differences of the parameters in each layer of the cell model.

The purpose of this smoothness criterion is to prevent lateral variations in density and slowness that are not necessary for fitting the data. Compared to the smoothness criterion used in standard inversion methods, in which W is set to zero, this criterion is much more effective in this regard.

2.5.3 Uniqueness

To understand the uniqueness of $\hat{p}$, we study its relationship to $\underline{p}$ by substituting Equation (33) into Equation (34) giving

$$\hat{\underline{p}} = A^+ A\underline{p} + A^+ \underline{e} \equiv R\underline{p} + A^+ \underline{e} .$$

This means that $\hat{\underline{p}}$ is an estimate for $R\underline{p}$ with error of estimation $A^+ \underline{e}$:

$$E(\hat{\underline{p}}) = R\underline{p}$$

$$Var\ (\hat{\underline{p}}) = A^+ A^{+T}\ . \tag{37}$$

The matrix R is called the resolution matrix. Equation (37) shows that each component of $\hat{\underline{p}}$ is an estimate for a weighted average of the components of $\underline{p}$. The weighting coefficients, called an "averaging kernel," are the components of the appropriate row of R.

Denote the ith averaging kernel (i^{th} row of R) by the vector $\underline{k}_i$. The extent to which $\underline{k}_i$ resembles the vector $\underline{\delta}_i$ (the ith row of the unit matrix) is a measure of the resolving power of the data $\underline{d}$ for determining the ith parameter p_i. In fact, an alternate way to define the optimal estimate $\hat{\underline{p}}$, is to let $\hat{p}_i = \underline{a}_i^T \underline{d}$ and minimize $r_i^2 + \alpha\,v_i^2$ for each i, where

$$r_i^2 = |B^{-1}\,(\underline{k}_i - \underline{\delta}_i)|^2 = |B^{-1}\,(A^T \underline{a}_i - \underline{\delta}_i)|^2$$

$$v_i^2 = Var\ (\hat{p}_i) = |\underline{a}_i|^2\ . \tag{38}$$

The quantities r_i and v_i describe the uniqueness of the estimate $\hat{p}_i$. The quantity r_i indicates how well the data resolve p_i with standard deviation v_i. It is convenient to define a normalized measure of resolving power by

$$q_i = 1 - (r_i / |B^{-1}\,\underline{\delta}_i|)^2\ . \tag{39}$$

q_i takes values from 0 to 1: $q_i = 0$ indicates no resolving power and $q_i = 1$ indicates perfect resolving power.

2.5.4   Computational Method

The generalized inverse A^+ was calculated with a matrix method known as singular value decomposition (SVD). The method takes advantage of the fact that any real M by N matrix can be decomposed as (Lanczos, 1961)

$$\underset{MxN}{C} = \underset{MxK}{S} \underset{KxK}{\Lambda} \underset{KxN}{T^T} \tag{40}$$

where K is the rank of C and obeys $K \leq \min (M,N)$. The matrix Λ is a square diagonal matrix containing the non-zero singular values of C:

$$\Lambda = \text{diag} (\lambda_1, \lambda_2, \ldots, \lambda_K) .$$

The K columns of the matrices S and T are left-hand and right-hand othornormal eigenvectors of C, respectively. Thus,

$$S^T S = I, \quad T^T T = I .$$

To find A^+, as defined in Equation (35), the matrix C is defined as

$$C = AB^{-1}$$

and decomposed as in Equation (40). Then, A^+ is given by

$$A^+ = B^{-1} T \Lambda (\Lambda^2 + \alpha I)^{-1} S^T . \tag{41}$$

It can be seen that the trade-off parameter α does not affect S, Λ, or T so they need only be calcaluted once. Furthermore, singular values that are small compared to $\alpha^{1/2}$ do not contribute

much to A^+, so every non-zero singular value and its associated eigenvectors need not be computed.

The trade-off parameter determines the number of degrees of freedom in the estimate $\hat{p}$. It can be seen from Equation (41) that as α approaches ∞, A^+ approaches zero in which case $\hat{p}$ is zero and has zero degrees of freedom. In general, the number of degrees of freedom is given by

$$f = \sum_{k=1}^{K} \frac{\lambda_k^2}{\lambda_k^2 + \alpha} . \tag{42}$$

In effect, f is the number of linearly independent combinations of the data vector $\underline{d}$ that are fit by $\hat{p}$.

The straightforward numerical implementation of SVD requires alternating operations on the rows and columns of C. Consequently, this procedure can be very inefficient unless C and other needed arrays can be simultaneously held in the internal memory of the computer. On the UNIVAC 1108, the largest matrix that can be decomposed in core is roughly 170 by 170 unless extended memory facilities are invoked. For the Imperial Valley inversion, the matrix involved was much larger than this (746 by 216). Therefore, it was necessary to develop and employ a pre-SVD procedure for reducing C by Householder transformations to a smaller matrix suitable for an in-core SVD routine. In addition, a post-SVD procedure was developed to reconstruct the eigenvectors of the original matrix C from the Householder transformations and the eigenvectors output by the SVD routine.

III. RESULTS

3.1 SMALL-GRID CORRECTION FOR THE IMPERIAL VALLEY SEDIMENTS

As noted in previous reports written under this contract
(Savino, et al., March, June 1977) and by other people who
have investigated teleseismic and gravity data from the
Imperial Valley (Steeples, 1975; Biehler, 1964), the near-
surface low velocity sediments in this region have a major
effect on both travel-time delays and the gravity field ob-
served there. Steeples (1975) estimated the delay through
the thickest section of the sediments as being approximately
0.8 seconds for vertical incidence and longer for shallower
angles of incidence. With respect to the gravity field,
Biehler (1964) showed that, because of the increase of density
with depth typical of a thick sedimentary basin, most of the
observed gravity anomaly in the Imperial Valley is caused by
the upper few thousand feet of sediments. Thus, it was clear
from the outset of this program that we would have to, in
effect, strip off the sediments to uncover details of the
deeper structure.

3.1.1 Sediment Thickness Model

Figure 6 is a depth-to-basement map of the Imperial
Valley taken from Rex (1970). Various kinds of geophysical
data were used to produce this map ranging from surface
mapping of major fault systems to refraction profiles and
information from deep wells. The basement depths in many
locations, however, are best guess estimates.

A digitized version of Figure 6 was obtained from
Professor Shawn Biehler. While the original digitization
was performed on a regular 2 km by 2 km grid, in view of the
scale lengths of the features of interest in this study we
smoothed the model to a 6 km by 6 km grid. This smoothing

46

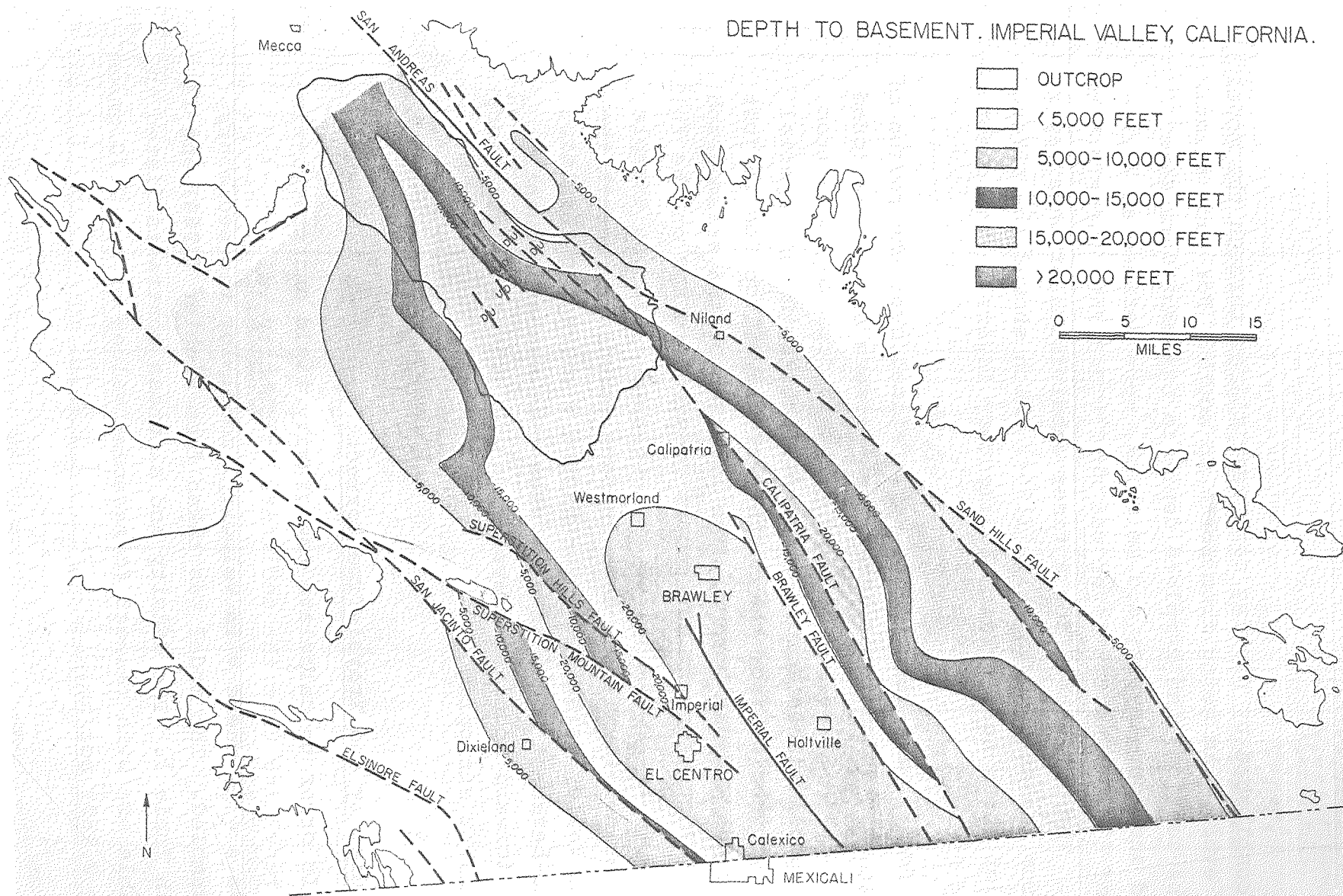DEPTH TO BASEMENT. IMPERIAL VALLEY, CALIFORNIA.

Figure 5. Map of the thickness of water filled sediments in the Imperial Valley. This may also be considered a depth to basement map with contours at 5000 feet increments.

was accomplished by picking east-west slices through the model
spaced every 6 km going from north to south. For each slice,
or cross-section, the complete depth to basement data were
plotted and four layers, 1.5 km thick, were defined at incre-
ments of 6 km. The top layer was subdivided into three 0.5 km
layers. The motivation for a finer subdivision of this layer
came from the study by Biehler (1964) which showed the strong
effect of these near-surface sedimentary layers to the observed
gravity field.

Twenty east-west slices were defined over the region of
interest from which layer interfaces between slices are found
by linear interpolation. Figure 7 shows, from top to bottom,
three typical slices (cross-sections) that span the Imperial
Valley, proceeding from the north near the Salton Sea to just
south of the Mexican border. The location of the seismograph
station SUP on basement outcrop as compared to SNR on the full
thickness of sediments (Slice 10 in Figure 7) is one example
of the variability in the near-surface structure beneath the
Imperial Valley seismic array. Figure 8 shows the resulting
depth-to-basement model in plan view that was subsequently
used in forward modeling travel-time and gravity calculations
for sediment stripping.

3.1.2 <u>Gravity and Travel-Time Corrections</u>

In order to calculate the gravity field and travel-time
delays resulting from the sediments, a density-velocity (or
slowness $a = \frac{1}{v}$, where v is velocity) model for the sediments
was assembled. The model was taken from Biehler (1964) and is
given in Table 1. The density and slowness contrasts listed in
this table are with respect to basement values of $\rho = 2.70$ gm/cm^3
and a = 0.1695 sec/km.

SLICE 20

SLICE 10

SUP   SNR
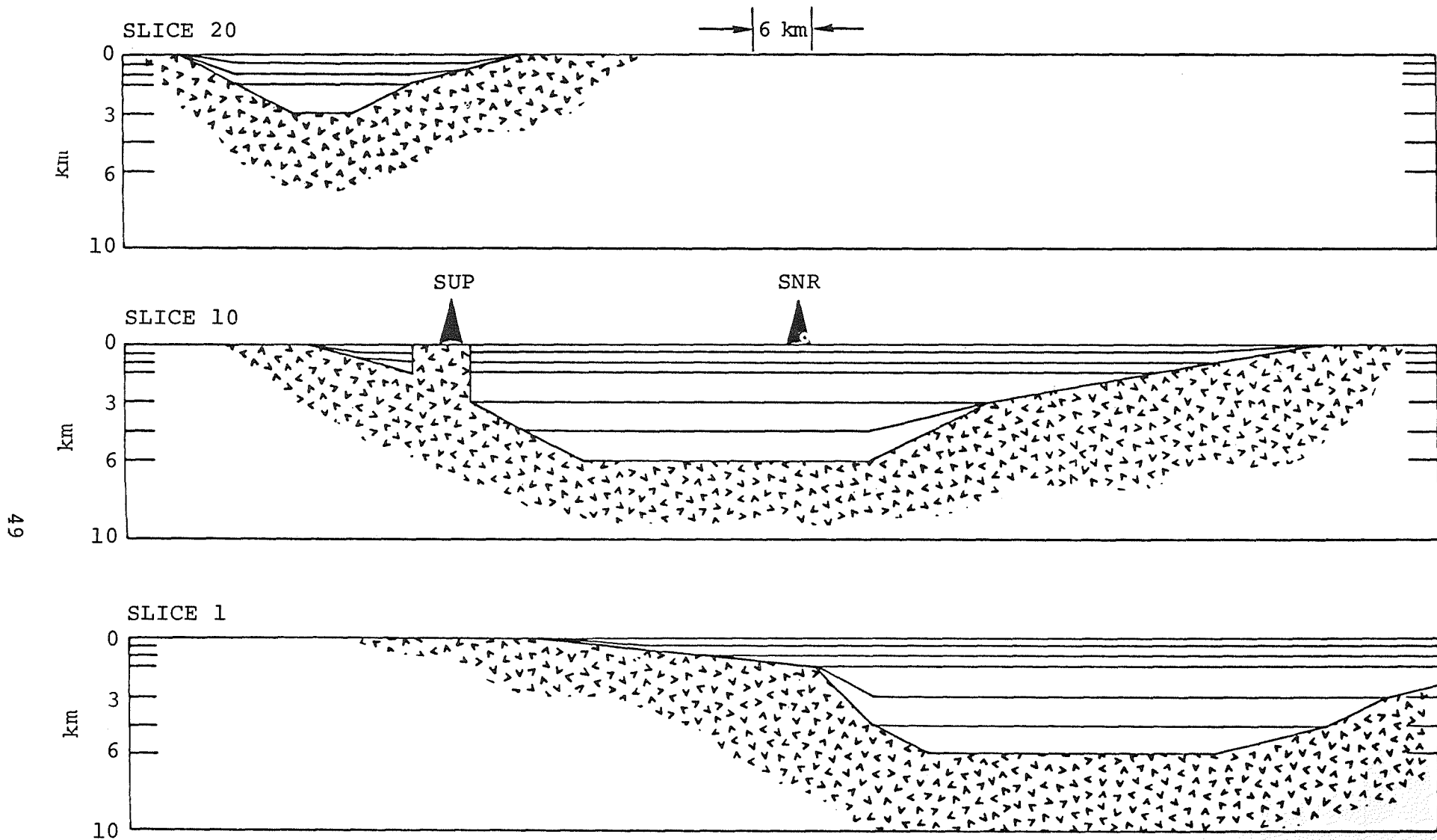
SLICE 1

6 km

km

49

Figure 7.   Cross-section and views of three east-west slices through the Imperial
Valley sediments. The slice at the top of this figure is representative
of the sediments near the Salton Sea. The next two slices represent the
sediments further to the south, with Slice 1 appropriate to sediments 20
to 30 km south of the Mexican border.

TABLE 1

DENSITY AND SLOWNESS SEDIMENT MODEL

Depth (km)	Density Contrast (gm/cm^3)	Slowness Contrast (sec/km)
0		
0.5	0.43	0.357
1.0	0.34	0.265
1.5	0.29	0.215
3.0	0.20	0.137
4.5	0.07	0.053
6.0	0.03	0.043

A gravity anomaly vector was computed using the density contrast model in Table 1 corresponding to the region in Figure 8. At each cell in the three-dimensional grid an element of the gravity kernel matrix was calculated using the formula for the gravitational attraction of a right rectangular prism given by Nagy (1966, 1967). The product of the kernel matrix with the model parameter vector, each element of which corresponds to a density contrast in a cell, results in a vector containing a value for the gravity anomaly at each point of observation (644 in this case). The data vector was subsequently low-pass filtered to minimize discretization effects. The resulting predicted gravity field for the sediments is shown in Figure 9.

A travel-time delay vector was computed for the sediment stack using the slowness model in Table 1. The delays were calculated for the actual azimuths and ray parameters corresponding to the observed events in the teleseismic data base. The results are shown in Figure 10 at three different azimuths for each of the 16 stations in the array.
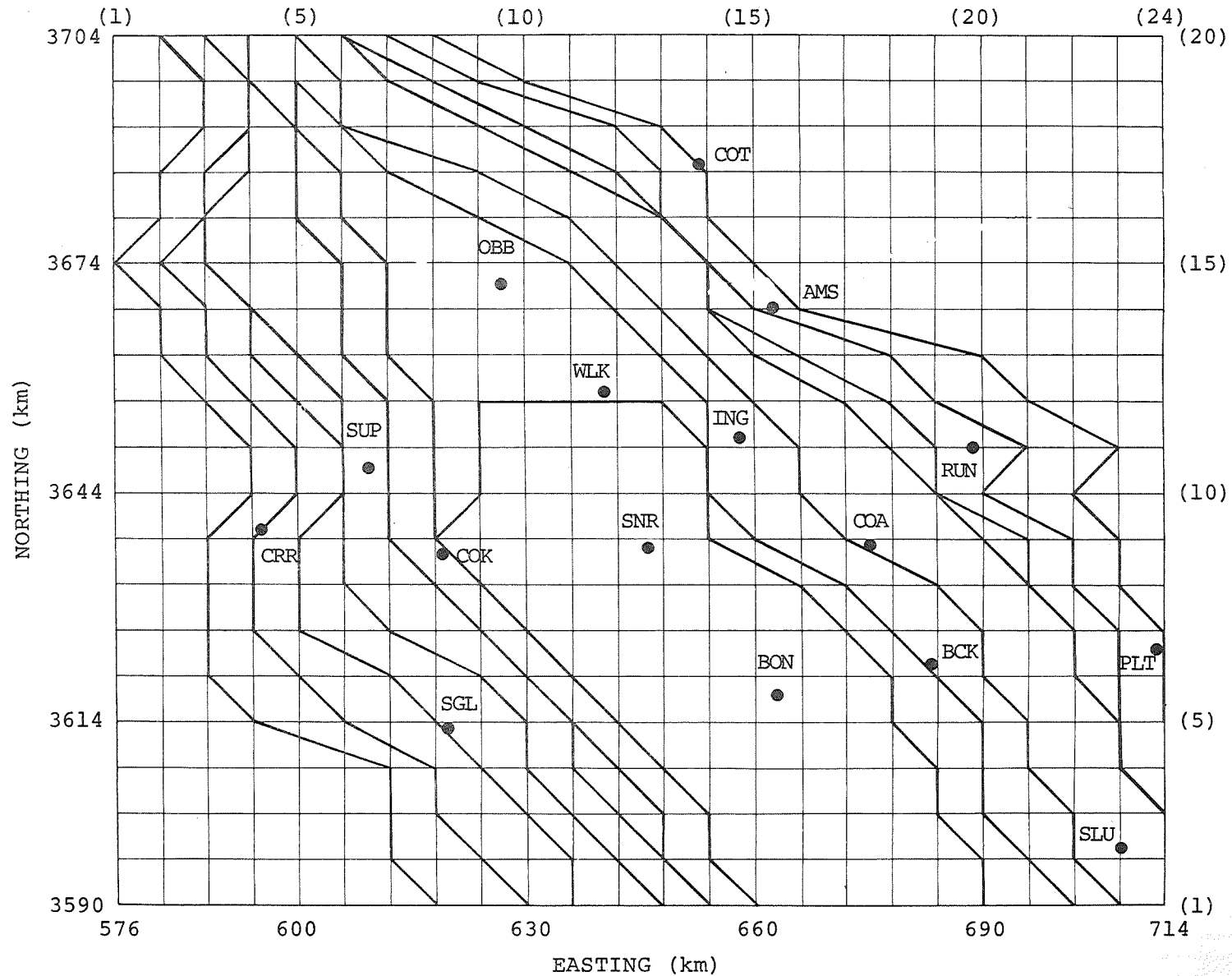
Figure 8. Smoothed version of depth-to-basement map used in the small grid calculations to effectively strip-off the sedimentary layers. Slice numbers are given inside the parentheses. The seismic stations are indicated by closed circles.
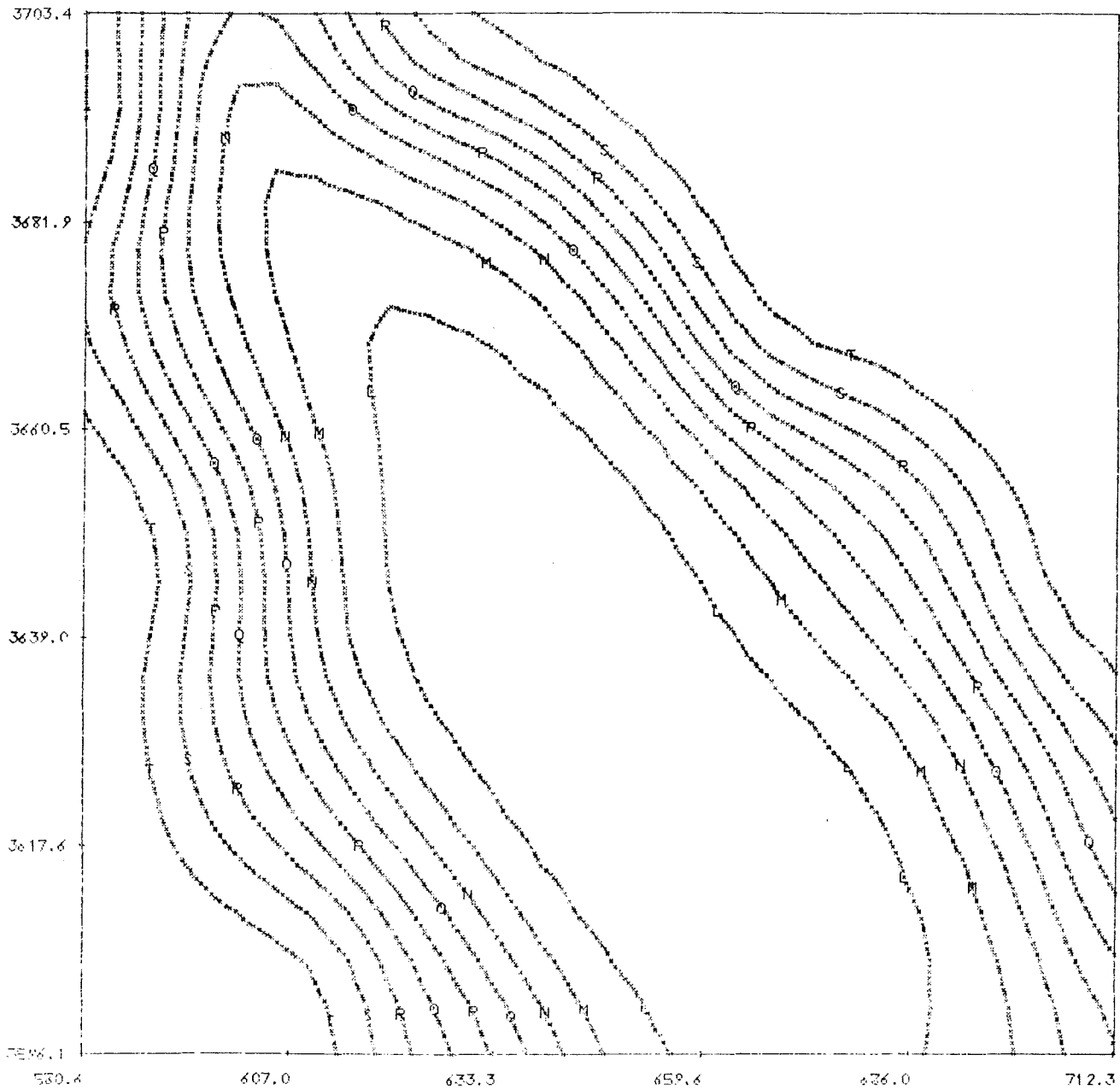
Figure 9. Result of the small grid forward modeling
          effort after completion of the low-pass
          filtering operation. Actual data plus
          1000 milligals is displayed.

52

Figure 10.   Travel-time delays introduced by the sedimentary
             layers. The circumference of each circle corre-
             sponds to a 0.0 second delay, while the radius is
             0.5 seconds. Maximum delays are about 0.8 seconds
             for station located in the center of the valley.
             Delays are shown at three different azimuths and,
             in general, do not exhibit a significant dependence
             on azimuth.

The circumference of the circles in Figure 10 corresponds to a delay of 0.0 seconds. Positive delays are drawn out from the circles, while negative delays are drawn in toward the center. The radius of a circle equals 0.5 seconds. As expected, all of the delays associated with the sediments are $\geq$ 0 and do not exhibit a marked dependence on azimuth at any of the 16 stations. This latter result is to be expected because of the near vertical incidence of the ray paths, especially as the top of the sediment column is approached. The delays range from values of about 0.8 seconds for stations near the center of the valley (e.g., WLK, SNR, BON) to values < 0.1 seconds at several of the flank stations (e.g., AMS, COT, SUP). This delay vector was applied to the travel-time data to arrive at a set of residuals stripped of the sediments. The final correction in this series was for the different station elevations as reported in Hill, et al., (1975b).

3.2   FINAL OBSERVED DATA VECTORS

3.2.1 Gravity Data

Each gravity value in the original data base was supplied in the form of a complete Bouguer corrected gravity observation. In order to integrate this data base into the inversion codes it was necessary to carry out the preliminary processing steps described in Section II. The first of these consisted of calculating gravity values on a regular rectangular grid of points based on the original irregularly spaced observations. This was done for a large area including the region to be modeled by the inversion plus surrounding bands of data. The surrounding data were required to facilitate application of various filtering techniques. Figure 11 is a contour plot of the grid point gravity values for the region to be modeled.

54

COMPLETE BOUGER ANOMALIES 1:192000 SCALE 4 MG LEVELS
A= 9.2000+02B= 9.2400+02C= 9.2800+02D= 9.3200+02E= 9.3600+02F= 9.4000+02G= 9.4400+02H= 9.4800+02
I= 9.5200+02J= 9.5600+02K= 9.6000+02L= 9.6400+02M= 9.6800+02N= 9.7200+02O= 9.7600+02P= 9.8000+02
Q= 9.8400+02R= 9.8800+02S= 9.9200+02T= 9.9600+02

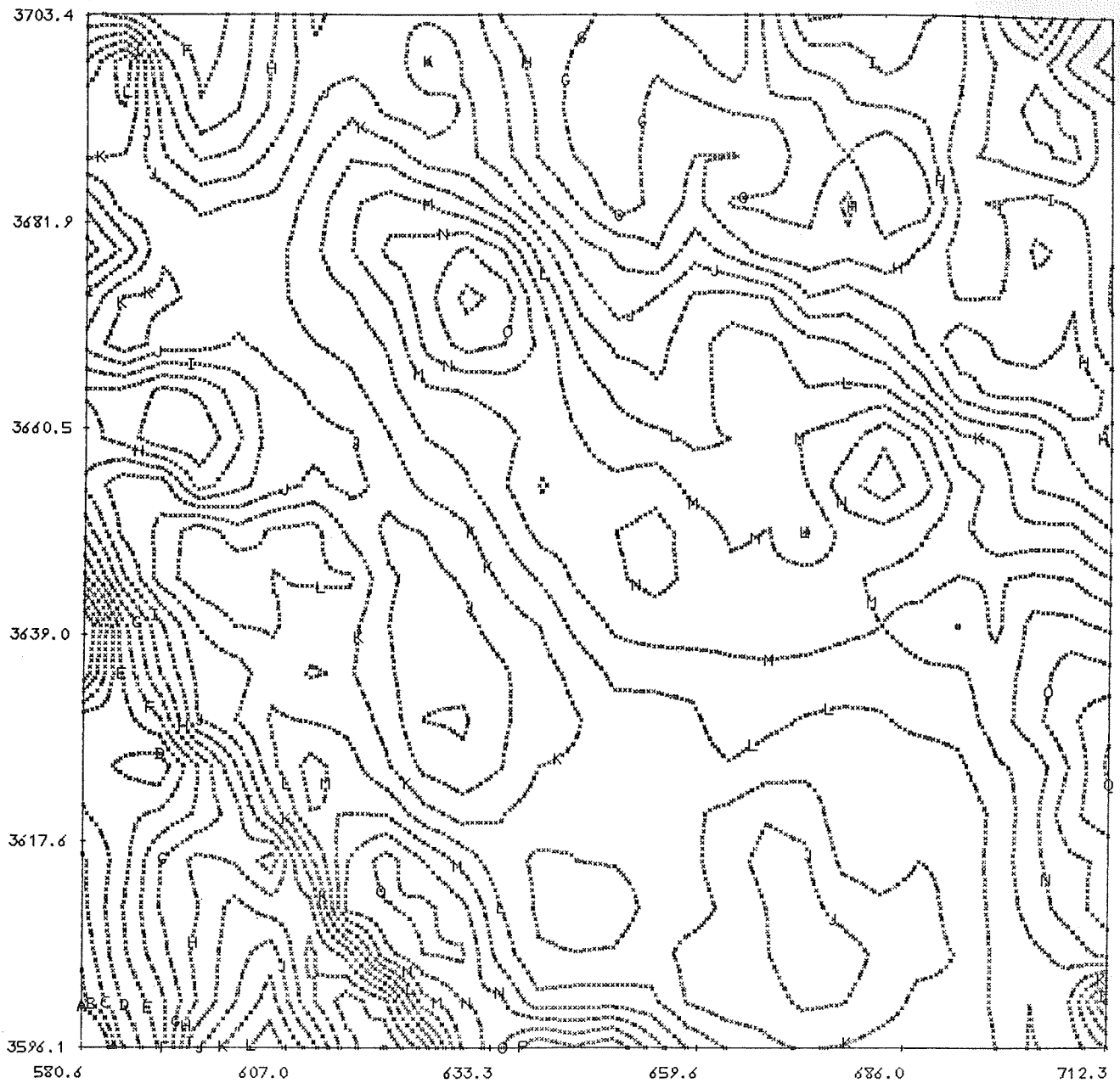

Figure 11.   Complete Bouguer anomalies interpolated to
              a regular grid (GPGV) before filtering.
              Contour levels are in milligals and the
              data plotted is the anomaly plus 1000
              milligals.

55

Various filtering techniques were investigated to pro-
duce a gravity data set appropriate for a discretized model.
This involved the removal of both regional and near-surface
effects that could not be attributed to the density variations
of a cell-model. In addition to the small-grid sediment cor-
rection, the most effective techniques for removing these
effects while retaining maximum information in the data were
found to be the low-pass filtering, decimation, and detrending
operations described in Section II.

A 10 km wide Gaussian filter was employed to low-pass
filter the gravity data. The output of this filter was
decimated to a final grid spacing of 6.9 km. This process
suppressed the significant gravity field that can be contri-
buted by very small density anomalies near the points of
observation. Without filtering, these contributions would
appear as a coherent, systematic source of error which is
unacceptable to the inversion method. The final gravity data
vector is essentially a point by point subtraction of the
low-pass filtered small-grid correction from the filtered
observed data and is shown in Figure 12. In the inversion
results, the same data is plotted in a different format.

3.2.2 Travel-Time Data

As mentioned in Section II, the worldwide events that
were analyzed for travel-times to the array of seismograph
stations in the Imperial Valley were grouped into events from
50 separate source regions. These 50 regions represented the
sampling of distinct ray paths, with respect to azimuth and
epicentral distance, available for this study. The resulting
travel-time residuals, referenced to SUP, are plotted in
Figure 13a.

BOUGER ANOMALIES - SMALL GRID CORRECTION 4MG LEVELS
A=-8.0000+01B=-7.6000+01C=-7.2000+01D=-6.8000+01E=-6.4000+01F=-6.0000+01G=-5.6000+01H=-5.2000+01
I=-4.8000+01J=-4.4000+01K=-4.0000+01L=-3.6000+01M=-3.2000+01N=-2.8000+01O=-2.4000+01P=-2.0000+01·
Q=-1.6000+01R=-1.2000+01S=-8.0000+00T=-4.0000+00U= 0.0000   V= 4.0000+00W= 8.0000+00X= 1.2000+01
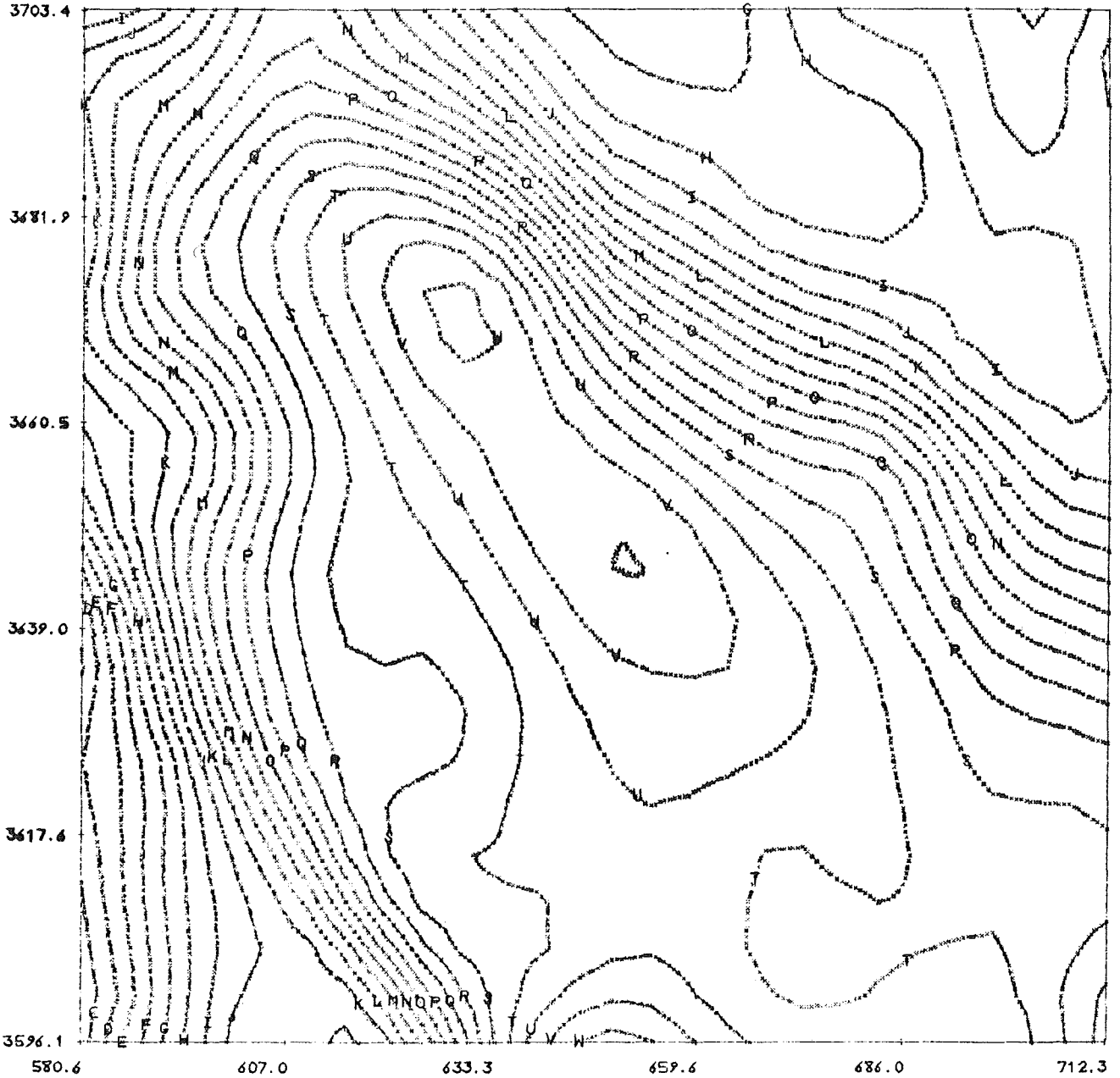
Figure 12.   Filtered gravity observations with the approximate
effect of sedimentary layers stripped off. The
result of the subtraction process is contoured in
milligals.

57
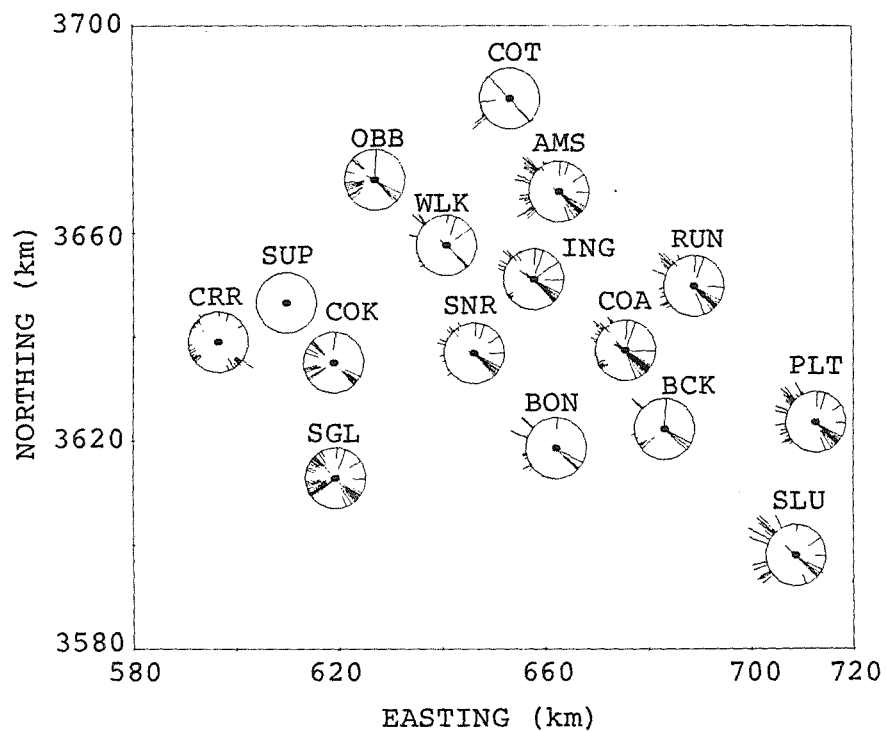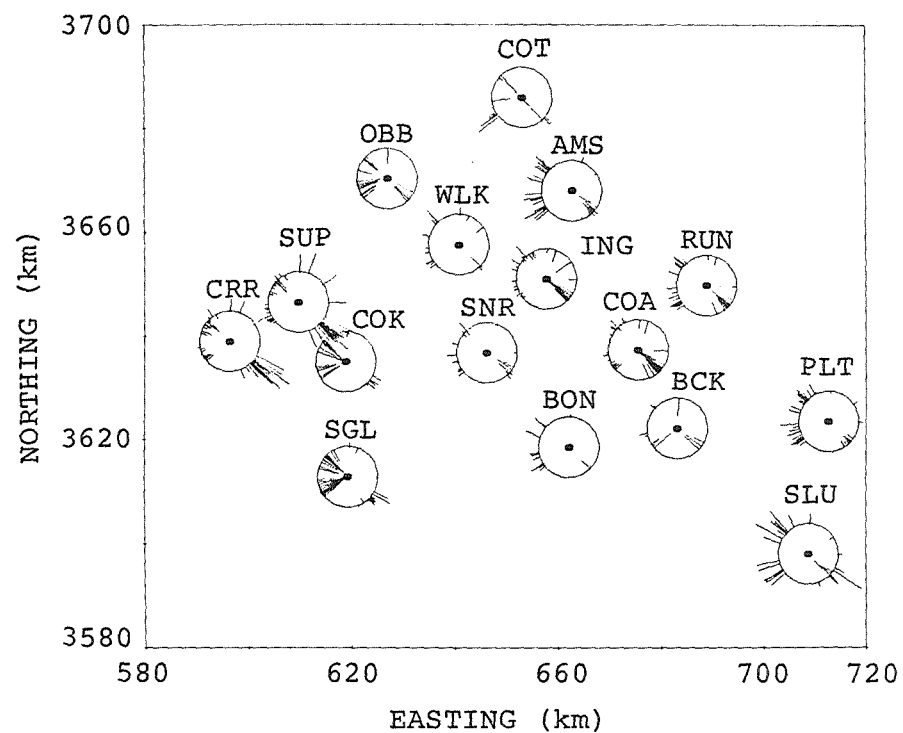
Figure 13.   (a) Travel-time residuals referenced to SUP. The small grid sediment correction has been applied to these data. The legend described in the caption to Figure 10 applies to this figure. (b) Travel-time residuals zero-meaned across all stations for each event group. The large azimuthal variation of most of these stations is quite apparent.

In this figure, positive residuals (late arrivals) are drawn out from the circumference of the cirles, while negative residuals (early arrivals) are drawn in toward the center of the circles. The circumference of each circle corresponds to a delay of 0.0 seconds and the lengths of the radii corresponds to a delay of 0.5 seconds. Note that the residuals plotted in Figure 13a were stripped of the delays resulting from the sediments by subtraction of the data shown previously in Figure 10.

The next step in processing the travel-time data was to zero-mean the data. The first procedure, discussed in Section 2.4.2, involved computing the variance-weighted mean value across all 16 stations for a particular event group and, then, subtracting this mean value from each of the individual station values. The results of this operation are shown in Figure 13b. The average-station relative residuals in this figure display an overall two-fold dependence on event group azimuth. For instance, the four stations (CRR, SUP, COK and SGL) located on the western flank of the array exhibit positive residuals (delays) for events originating at azimuths between 0 and 160 degrees, and negative residuals for event azimuths between 200 to 300 degrees. All of the remaining stations, with the exception of OBB, exhibit a residual pattern, however, which is just the opposite. A strong azimuthal variation in station residual arises from structure which is presumed to be deeper than the maximum depth (33 km) of the model to be inverted. Thus, we sought an additional zero-meaning procedure that would minimize the pronounced azimuthal variations evident in Figure 13b, and, as a result, the dependence in these residual data on deep structure.

In Figure 14, the results of this additional zero-meaning scheme, suggested by the data in Figure 13b, are plotted. Here, stations CRR, SUP, COK and SGL were zero-meaned separately from the remaining 12 stations. As the data in this figure clearly show, this zero-meaning scheme
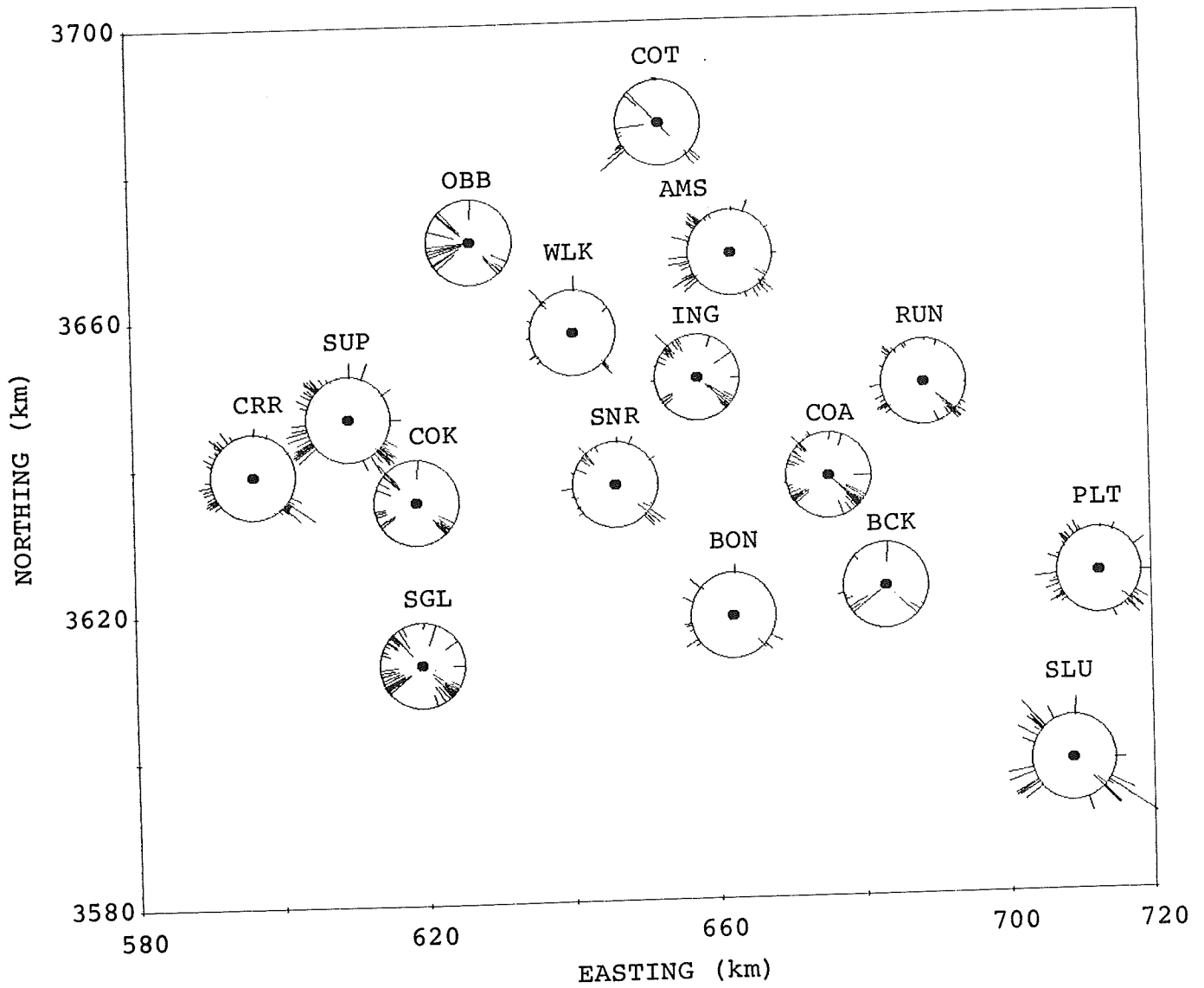
Figure 14. Travel-time residuals zero-meaned across two groups of stations for each event group. One station grouping consisted of SUP, CRR, COK and SGL. Most of the azimuthal variation seen in the two previous figures is gone.

has successfully minimized the azimuthal variation, at least to within the estimated variance of the residuals. These data comprise the travel-time vector in a form appropriate for input to the inversion codes.

3.3   INVERSION RESULTS

3.3.1 Model Parameterization

We modeled the crust and topmost mantle beneath the Imperial Valley as a four layer cell-model, each layer consisting of an eight by nine grid of cells (Figure 15). Lateral variations in density and slowness were assumed to exist only between 6 and 33 km, except for the upper 6 km of sediments for which the data were corrected. The velocities shown in Table 2 represent the plane-layered compressional velocity model used to calculate ray paths for the travel-time kernel matrix.

TABLE 2

LAYERING AND REFERENCE VELOCITIES FOR INVERSION MODEL

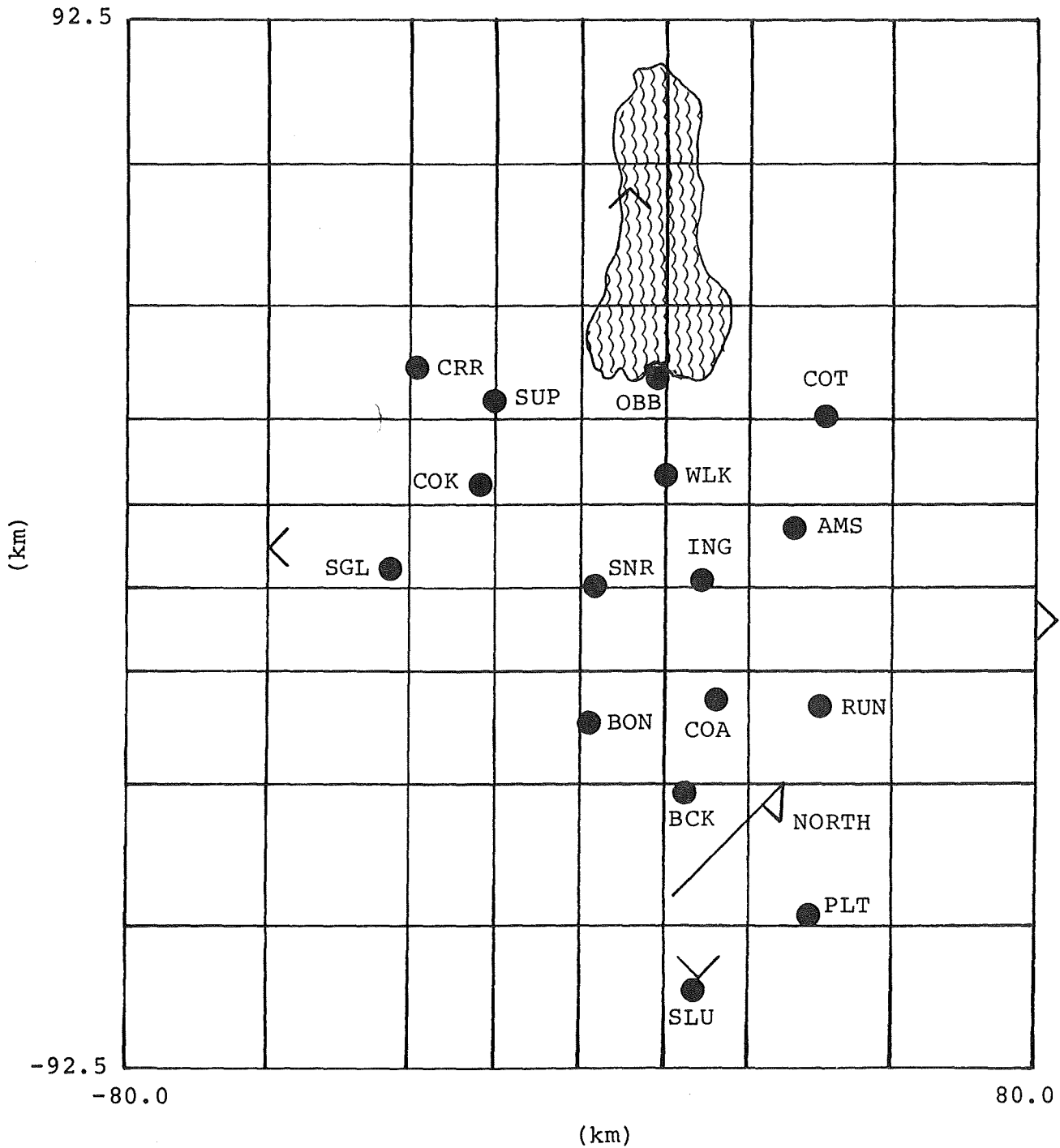| DEPTH (km)	LAYER	REFERENCE VELOCITY (km/s)
0.0		
	1	5.9
6.0		
	2	6.2
15.0		
	3	6.4
24.0		
	4	6.5
33.0		

Figure 15. Plan view of inversion model cell boundaries. The seismic stations and corners of the gravity grid are indicated for reference. The model extends beyond the area of data coverage in order to accommodate all density and velocity variations that affect the data. The outer rows of cells were treated as semi-infinite by the inversion.

The density-velocity relation assumed in the inversion was

$$\Delta \rho(\ell) = 0.4 \ \Delta v(\ell) \ , \quad \ell = 2,3,4,$$

where ℓ is layer number. This was translated to the following density-slowness relation:

$$\Delta \rho(\ell) = -0.4 \ v_o(\ell)^2 \ \Delta a(\ell) \ , \quad \ell = 2,3,4,$$

where $v_o(\ell)$ is the velocity in layer ℓ of the reference model. Our original intention was to use a $\Delta \rho$ to Δv ratio closer to the 0.3 value suggested by Press and Biehler (1964). However, our preliminary forward modeling results and other available information about the deep structure beneath the Imperial Valley indicated that because of crustal thinning, the true average velocity in each layer of our model was higher than the crustal reference value v_o. Thus, a $\Delta \rho$ to Δv ratio of 0.4 implied a reasonable $\Delta \rho$ to Δa ratio.

3.3.2 Preliminary Modeling

Two procedures were employed to obtain preliminary models of the Imperial Valley. The first was a formal inversion of the observed data without the benefit of a starting model. The second procedure was to forward model trial density-slowness structures, comparing their predicted data to the observed data. The results of these two procedures were used to construct a starting model to be input to a final inversion of the observed data.

The inversion with no starting model produced several optimal models, corresponding to different numbers of degrees

of freedom between 10 and 120. The smoothest model giving an
acceptable fit to the data had 80 degrees of freedom and is
shown in Figure 16 as contour plots of the density variations
in each of the three layers between 6 and 33 km. The gravity
and travel-time data predicted by this model are nearly identi-
cal to the data predicted by the final model, which are shown
later in Figure 19.

Two main points were concluded from this preliminary
inversion. First, a good match to both the gravity and travel-
time data (Figure 19) is provided by a model forced to obey
a fixed density-velocity relation. Second, the lateral density
and velocity contrasts needed to fit the observed data are
large: greater than 0.3 gm/cm^3 and 0.75 km/s, respectively, as
seen in Figure 16. These large contrasts are almost certainly
due to the difference between crust and mantle materials.
Therefore, the most feasible explanation for most of the
observed gravity and travel-time anomalies is lateral variations
in crustal thickness.

The preliminary inversion model is a nonunique solution
for the density-velocity structure beneath the Imperial Valley.
Its essential features, and the results of forward modeling,
were next incorporated into a starting model for the purpose
of reducing the nonuniqueness of a final inversion and pro-
ducing a more realistic model. The starting model, shown in
Figure 17, is a simplified model of a crust with variable
thickness and, in addition, has no anomalies shallower than
15 km. It predicts only the gross features of the observed
data but, compared to the model of Figure 16, it concentrates
more high density material in the deepest layer and is thus a
more tenable model of crustal thickness variation.

64

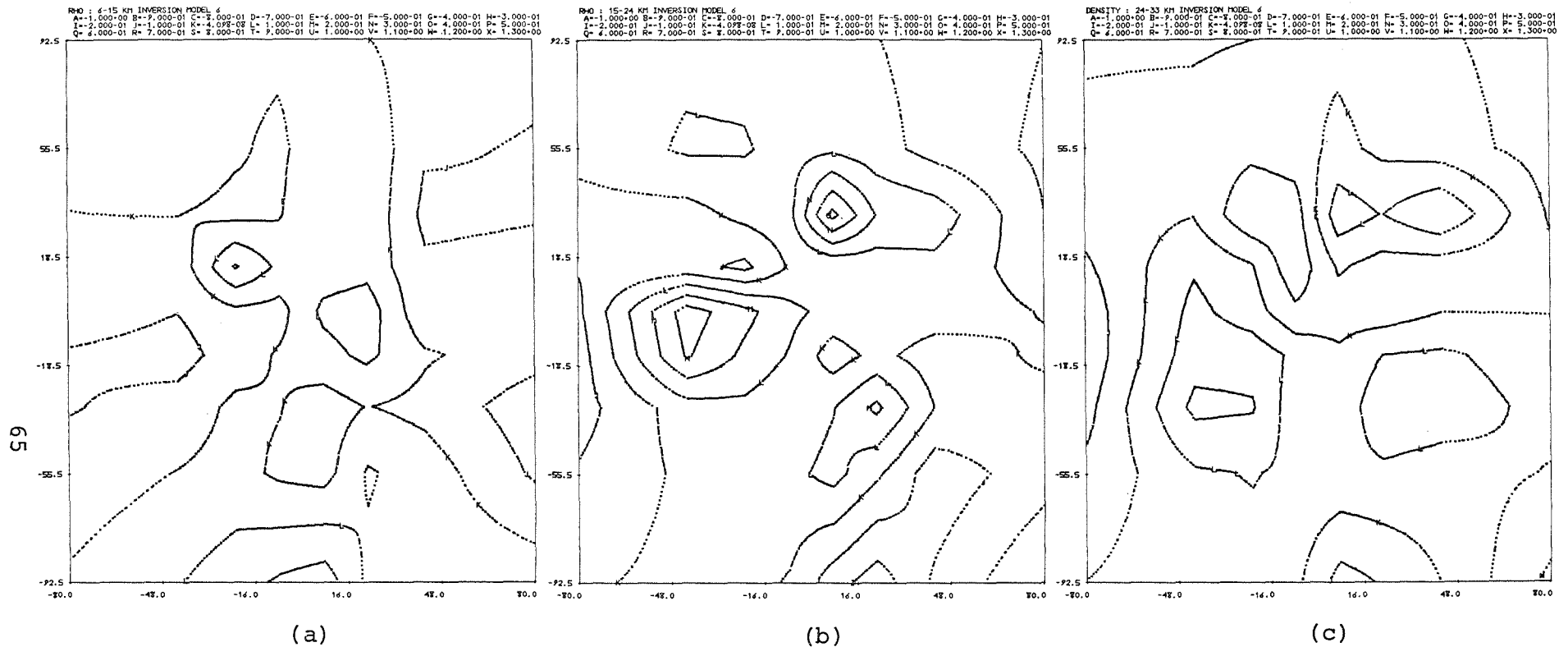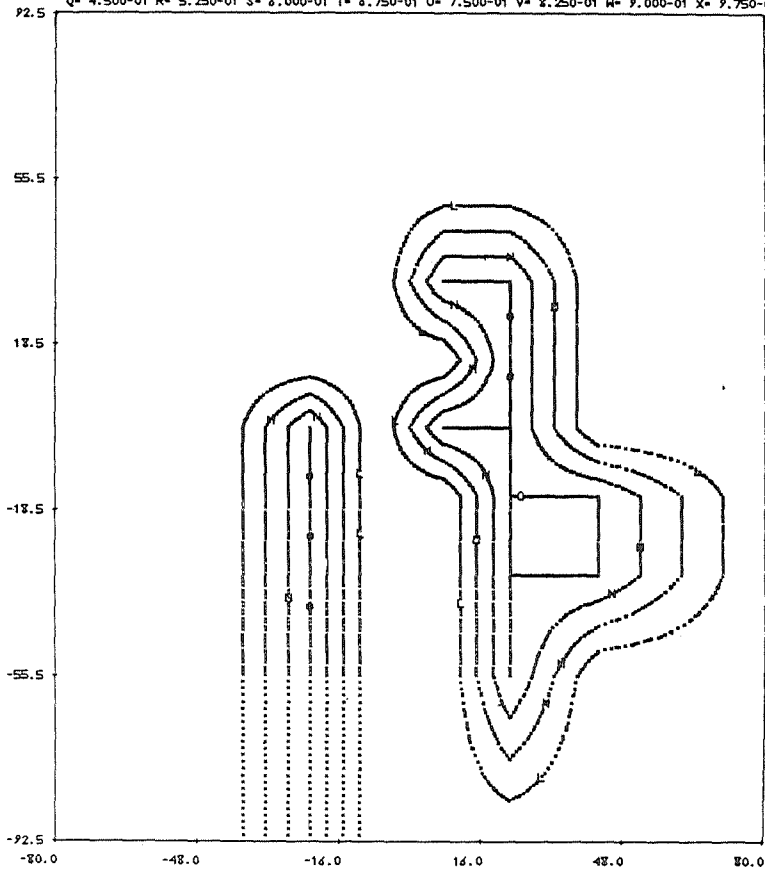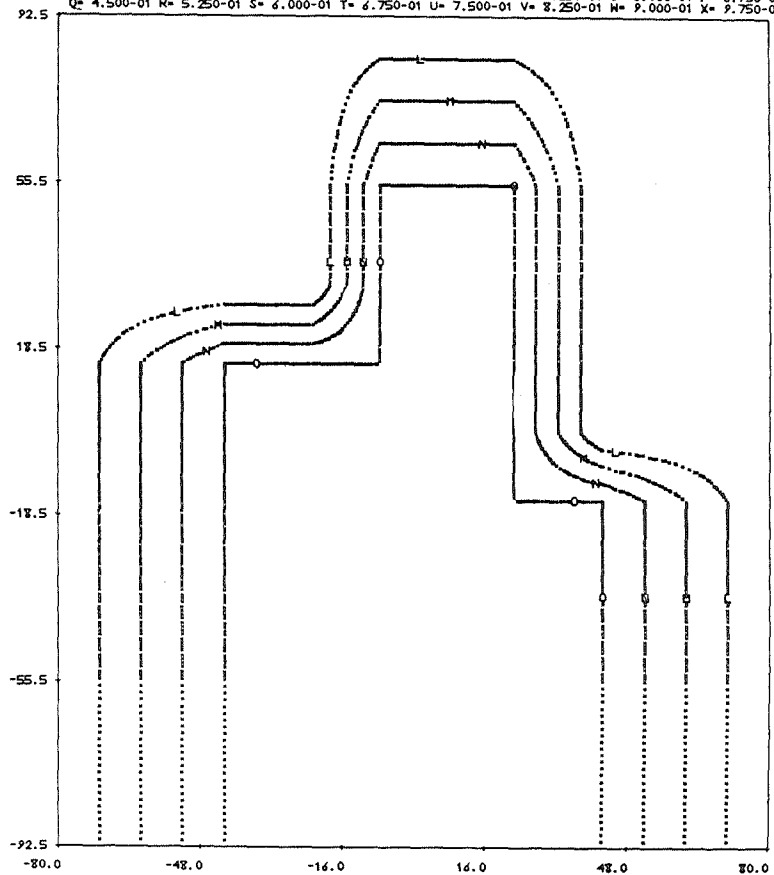Figure 16. Preliminary inversion density model for the three layers with depth ranges (a) 6 to 15 km, (b) 15 to 24 km, and (c) 24 to 33 km. Contour interval in each plot is 0.1 gm/cm^3. Each plot covers the 160 by 185 km area of cells shown in Figure 15.

Figure 17. Starting density model used in final inversion for the two layers with depth ranges (a) 15 to 24 km and (b) 24 to 33 km. Contour interval is 0.075 gm/cm³.

3.3.3 Final Inversion

Figure 18 displays our final model obtained by inverting the combined gravity and travel-time data set with the model in Figure 17 as a starting model. Like the preliminary inversion model, the final model has 80 degrees of freedom. The data predicted by the final model (Figure 19) are nearly the same as the data predicted by the preliminary inversion model. This was expected since for a given number of degrees of freedom, a starting model does not greatly affect the data predicted by the final model when the data functionals are linear.

Figure 19 shows that the final model fits the observed gravity data very well. Over most of the region, the predicted and observed gravity data agree to within 4 milligals as compared to the 60 milligals anomaly in the observed data. In the case of the travel-time data (Figure 19b), the final model accounts for most of the observed anomalies, both in magnitude and azimuthal dependence. Due to the scatter in the 527 observed residuals, it is clearly not possible to fit the details of the azimuthal variation. However, the overall agreement between the observed and predicted travel-times is good, particularly for the stations with the most reliable data. An inversion model is expected to give the best fit to data at stations with the most accurate and largest number of data. In the case of the Imperial Valley array, the stations in the center of the valley produced the fewest usable data, as can be seen in Figure 19b and in Figure 20, which shows the percentage of events recorded by each station from the total of 182 events used in this study. As a result, the agreement between the predicted and observed residuals is better for the flank stations than the central stations. One notable exception to this is the failure of the final model to simultaneously predict both the large positive residuals for southeast azimuths at Station SUP and the large negative residuals for the northwest azimuths at COK.

DELTA RHO : 6-15 KM INVERSION MODEL 6A
A=-7.500-01 B=-6.750-01 C=-6.000-01 D=-5.250-01 E=-4.500-01 F=-3.750-01 G=-3.000-01 H=-2.250-01
I=-1.500-01 J=-7.500-02 K=-2.142-08 L= 7.500-02 M= 1.500-01 N= 2.250-01 O= 3.000-01 P= 3.750-01
Q= 4.500-01 R= 5.250-01 S= 6.000-01 T= 6.750-01 U= 7.500-01 V= 8.250-01 W= 9.000-01 X= 9.750-01

DELTA RHO : 15-24 KM INVERSION MODEL 6A
A=-7.500-01 B=-6.750-01 C=-6.000-01 D=-5.250-01 E=-4.500-01 F=-3.750-01 G=-3.000-01 H=-2.250-01
I=-1.500-01 J=-7.500-02 K=-2.142-08 L= 7.500-02 M= 1.500-01 N= 2.250-01 O= 3.000-01 P= 3.750-01
Q= 4.500-01 R= 5.250-01 S= 6.000-01 T= 6.750-01 U= 7.500-01 V= 8.250-01 W= 9.000-01 X= 9.750-01

DELTA RHO : 24-33 KM INVERSION MODEL 6A
A=-7.500-01 B=-6.750-01 C=-6.000-01 D=-5.250-01 E=-4.500-01 F=-3.750-01 G=-3.000-01 H=-2.250-01
I=-1.500-01 J=-7.500-02 K=-2.142-08 L= 7.500-02 M= 1.500-01 N= 2.250-01 O= 3.000-01 P= 3.750-01
Q= 4.500-01 R= 5.250-01 S= 6.000-01 T= 6.750-01 U= 7.500-01 V= 8.250-01 W= 9.000-01 X= 9.750-01

(a)

(b)

(c)

Figure 18.   Final inversion density model for the three layers with depth ranges
(a) 6 to 15 km, (b) 15 to 24 km, and (c) 24 to 33 km.
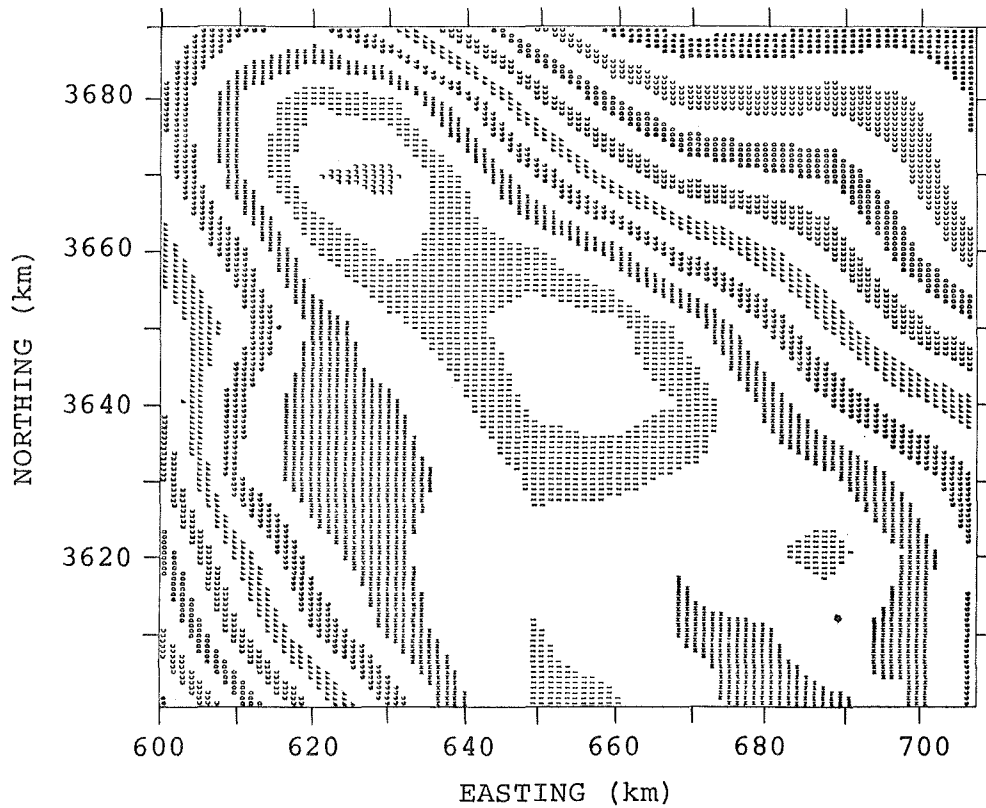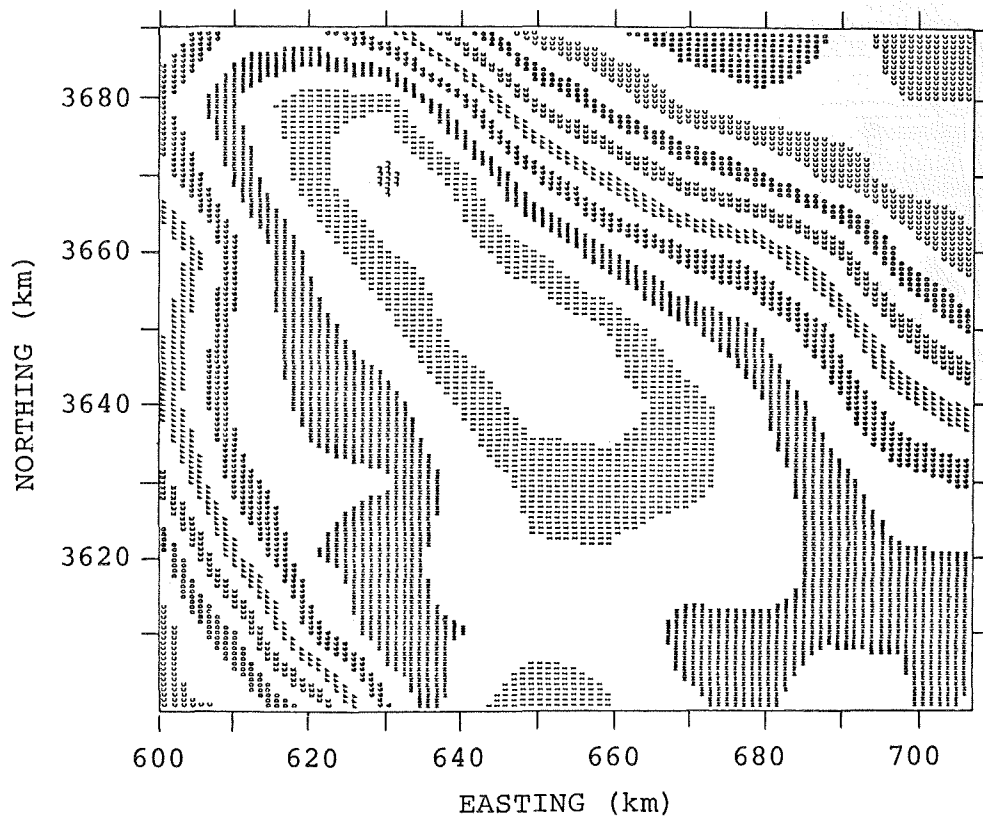
Figure 19a. Comparison of observed gravity data (top) and gravity data predicted by final inversion model (bottom). Each band of symbols or blank area defines a 4 milligal range. C denotes -48 to -44 milligals. J denotes 8 to 12 milligals.
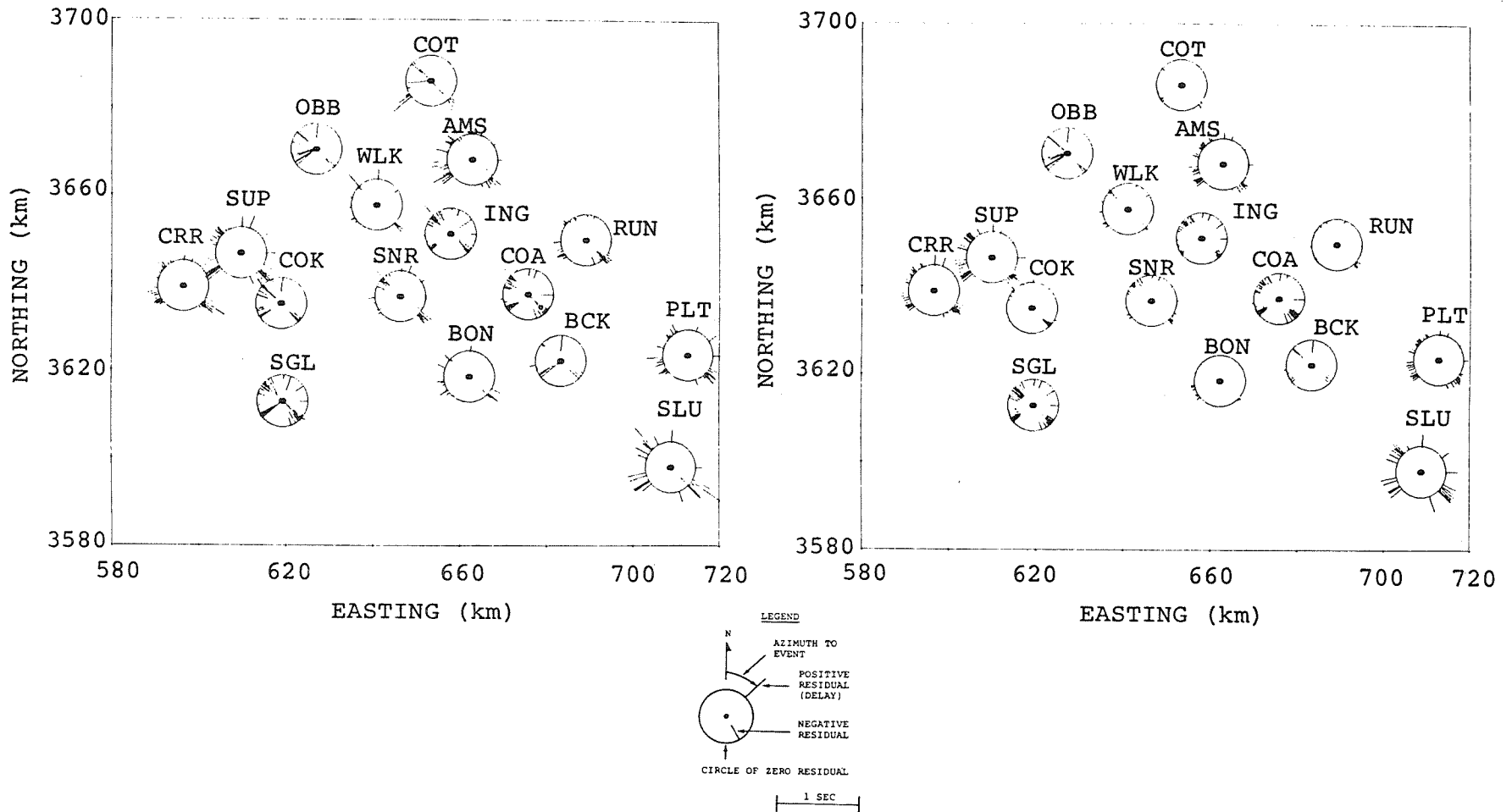
Figure 19b. Comparison of observed relative travel-time residuals (left) and relative travel-time residuals predicted by final inversion model (right). Circle radius is equal to 0.4 s.
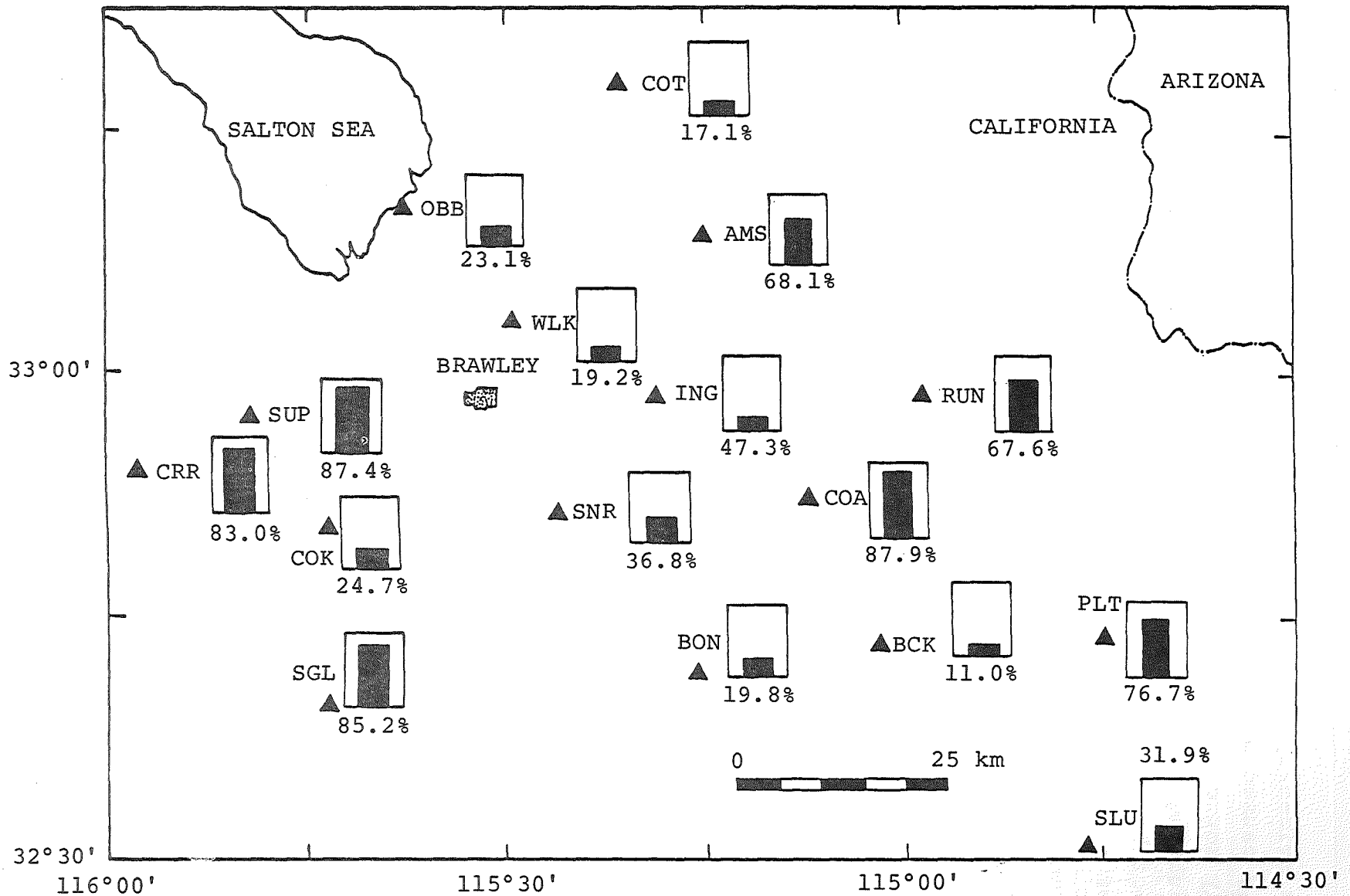
Figure 20. Percentage of the 182 total events recorded by each of the 16 Imperial
Valley array stations. This figure demonstrates the two-fold nature
of this array; the high event reporting flank stations versus low event
reporting stations in the valley.

This is evidently due to an inconsistency in the observed data possibly caused by a systematic error in the COK residuals. A likely source of this error is the complexity of the faulting and resulting sediment thickness near COK (Figure 6) which could not be accounted for in the small-grid correction because of a lack of detailed information in this area.

The final model (Figure 18) is a good example of an optimal inversion model. In addition to providing a good fit to the data, it is smooth in that it contains no unnecessary large lateral variations and is coherent from layer to layer. Compared to the preliminary inversion model, the final model has smaller density contrasts at depths shallower than 15 km and a broader area of high-density, high-velocity material below 15 km. It is thus consistent with an interpretation in terms of variations in crustal thickness.

To properly interpret the final model, we must examine its uniqueness. Figure 21 shows contour plots of the nomalized resolving power (q) in each layer. In Section 2.5.3 we saw that q can assume values between zero and one, where zero indicates the worst possible, and one the best possible, resolving power. For our cell model, "perfect" resolving power, or $q = 1$, would imply that the data determined gravity and velocity variations on a scale less than or equal to the dimensions of the cells. In general, a rule of thumb is that the data resolve variations on a scale equal to $1/q$ times the cell dimensions, which are 9 by 15 by 15 km in the center of the model.

The resolving power of a gravity data set is mainly a function of its areal coverage and station spacing. Station spacing smaller than the minimum depth of investigation essentially achieves the maximum resolution possible from gravity data. The travel-time residuals observed at an array of stations measure differences in the integrated slowness along the ray paths to different stations. Their resolving

Figure 21. Normalized resolving power of combined gravity/travel-time data set in the three layers of inversion model with depth ranges (a) 6 to 15 km, (b) 15 to 24 km, and (c) 24 to 33 km.
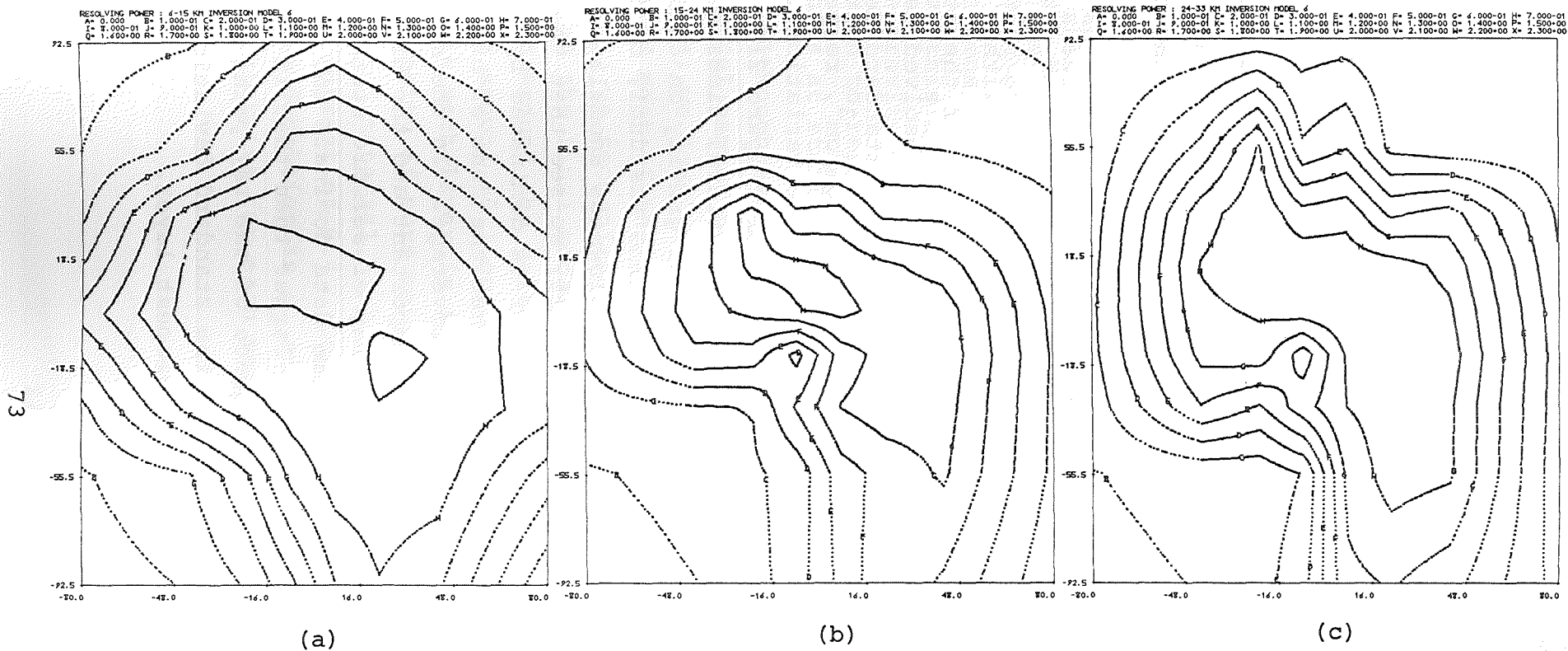
power is controlled by three factors. The first is an inherent limitation caused by the finite wavelength of the observed signals. The second is the array configuration, both its areal coverage and station spacing. Third is the distance and azimuthal distribution of the observed events. The latter two factors determine the extent to which the subsurface region of interest is probed by the ray paths of the observed signals. It was these two factors that determined the resolving power contributed by the travel-time data in this study.

Figure 21 shows that the resolving power exceeds 0.7 in the central portion of each layer in the model. For the most part, the largest variations in density are within the regions for which q exceeds 0.5. Our analysis of the standard deviations of the model showed that the best resolved density variations in each layer are determined with standard deviations of approximately 0.02, 0.03 and 0.03 gm/cm^3, respectively, which are small compared to magnitude of the variations.

The distribution of resolving power (Figure 21) reflects the manner in which gravity and travel-times sense subsurface anomalies. The dependence of gravity on density decays rapidly with depth. A travel-time residual, on the other hand, is equally sensitive to slowness anomalies everywhere along its ray path. As a result, we see that the resolving power in the shallowest layer is dominated by the gravity data as indicated by the fact that the zone of high resolution roughly outlines their areal coverage. In the middle layer, the gravity data are less important and the high resolution zone tends to outline the array of seismic stations. In the deepest layer, the travel-time data dominate and define a zone of high resolution somewhat larger than that in the middle layer, partly due to the divergence of the ray paths with depth and partly due to the fact that the standard deviations of the model tend to be larger in the deepest layer.

Because of their different sensitivities to depth varia-
tions in density or slowness, the combined inversion of gravity
and travel-time data reduces much of the poor depth resolution
both gravity and travel-times have when inverted separately.
However, it does not eliminate the depth resolution problem
completely, so the depths of density and velocity anomalies
can be mislocated to some extent, even in a combined inversion.
There is some evidence of this in our final model where there
is an apparent misalignment of the anomalies in different
layers. Moreover, in the shallowest layer, the density high
just west of the center of the layer is partially compensated
by the density low directly below it in the middle layer. We
believe this apparent vertical instability was not required
by the gravity data but might represent an attempt by the
inversion to resolve the conflict between the travel-time
residuals at stations COK and SUP, referred to earlier.

Although every density and velocity variation in our
final model cannot be attributed to a variation in crustal
thickness, we constructed a crustal thickness model that
explained most of the lateral variations. To define crustal
thickness, we recognized that in both the middle and bottom
layers of the final model, the largest values of density
clustered around the value 0.3 gm/cm^3 and the smallest values
clustered around -0.1 gm/cm^3. Since the average value of
density in each layer is indeterminate, we could treat 0.3
as the density of pure mantle and -0.1 as the density of
pure crustal material, implying a reasonable crust-mantle
density contrast of 0.4. Denoting these baseline-removed crust
and mantle densities as ρ_C and ρ_M, respectively, we defined the
crustal thickness for each vertical column of cells as

$$t = z_1 + \frac{h}{\rho_M - \rho_C} \sum_{\ell=1}^{3} \left(\rho_M - \hat{\Delta\rho}(\ell) \right),$$

where z_1 is the depth to top of the shallowest inverted layer (6 km), h is the thickness of the layers (9 km), and $\hat{\Delta\rho}(\ell)$ is the density estimate for the ℓth cell in the column.

The resulting crustal thickness model is contoured in Figure 22a and shown in Figure 22b in block form where each block corresponds to a column of model cells. A smoothed representation of this block model was shown earlier in Figure 3a. The model implies that crustal thickness ranges between approximately 6 and 33 km. However, this range depends on the values chosen for ρ_M and ρ_C. Table 3 lists the minimum and maximum crustal thickness values that result from a selection of reasonable values for ρ_M and ρ_C, including the values $\rho_M = 0.3$, $\rho_C = -0.1$ used for Figure 22.

TABLE 3

CRUSTAL THICKNESS RANGES FOR SELECTED VALUES OF
ρ_M and ρ_C, THE MANTLE AND CRUSTAL DENSITIES
ASSOCIATED WITH THE FINAL INVERSION MODEL

ρ_M	ρ_C	Minimum Thickness	Maximum Thickness
0.3	-0.1	6.2	33.3
0.4	-0.1	11.6	33.2
0.3	0.0	6.3	42.4
0.4	0.0	13.0	40.0

CRUSTAL THICKNESS: INVERSION 4A
A= 0.000   B= 1.500+00 C= 3.000+00 D= 4.500+00 E= 6.000+00 F= 7.500+00 G= 9.000+00 H= 1.050+01
I= 1.200+01 J= 1.350+01 K= 1.500+01 L= 1.650+01 M= 1.800+01 N= 1.950+01 O= 2.100+01 P= 2.250+01
Q= 2.400+01 R= 2.550+01 S= 2.700+01 T= 2.850+01 U= 3.000+01 V= 3.150+01 W= 3.300+01 X= 3.450+01

(a)

(b)

W

E

S

Z = 50 km
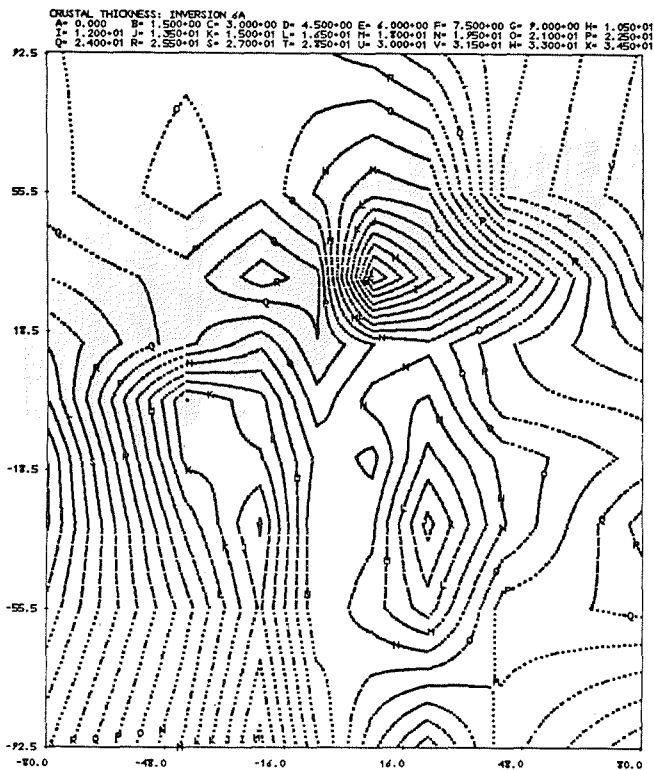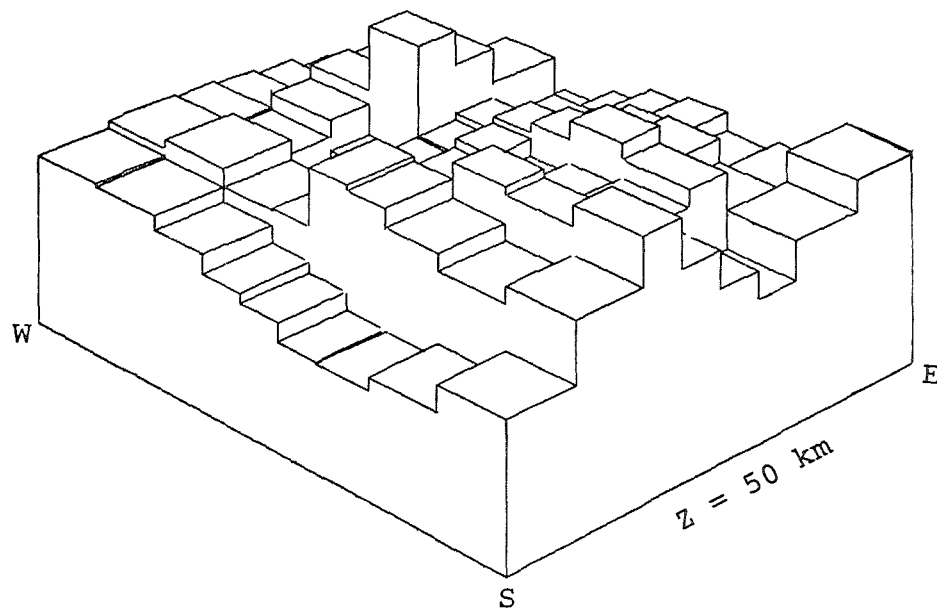
Figure 22.   (a) Contour map of crustal thickness model obtained by interpreting
0.3 gm/cm^3 in inversion model as mantle density and -0.1 gm/cm^3 as
crustal density.   Contour interval is 1.5 km.   (b) Perspective view
of block crustal thickness model as seen from due south of center
of model.

V. REFERENCES

Aki, K., A. Christoffersson and E. S. Husebye, (1977), "Determination of the Three-Dimensional Seismic Structure of the Lithosphere," J. Geophys. Res., 82, 277.

Atwater, T., (1970), "Implications of Plate Tectonics for the Cenozoic Evolution of Western North America," Geol. Soc. Amer. Bull., 81, 3513.

Backus, G. and F. Gilbert, (1970), "Uniqueness in the Inversion of Inaccurate Gross Earth Data," Phil. Trans. Roy. Soc. (London), Ser. A., 266, 123.

Biehler, S., (1964), "Geophysical Study of the Salton Trough of Southern California," Ph.D. Thesis, California Institute of Technology.

Combs, J. and D. Hadley, (1977), "Microearthquake Investigation of the Mesa Geothermal Anomaly, Imperial Valley, California," Geophysics, 42, 17.

Elders, W. A., R. W. Rex, T. Meidav, P. T. Robinson and S. Biehler, (1972), "Crustal Spreading in Southern California," Science 178, 15.

Hill, D. P., (1977), "A Model for Earthquake Swarms," J. Geophys. Res., 82, 1347.

Hill, D. P., P. Mowinchkel and L. G. Peake, (1975a), "Earthquakes, Active Faults, and Geothermal Areas in the Imperial Valley, California," Science, 188, 1306.

Hill, D. P., P. Mowinckel and K. M. Lahr, (1975b), "Catalog of Earthquakes in the Imperial Valley, California, June 1973 - May 1974," U.S. Geological Survey Open-File Report 75-101.

Jordan, T. H., (1973), "Estimation of the Radial Variation of Seismic Velocities and Density in the Earth," Ph.D. Thesis, California Institute of Technology.

Lanczos, C., (1961), Linear Differential Operators, Van Nostrand, New York.

Larson, R. L., H. W. Menard, and S. M. Smith, (1968), "Gulf of California: A Result of Ocean Floor Spreading and Transform Faulting," Science, 161, 781.

V. REFERENCES (continued)

Lomnitz, C., F. Mooser, C. Allen, J. N. Brune, and W. Thatcher, (1970), "Seismicity of the Gulf of California Region, Mexico - Preliminary Results," Geofis. Int., 10, 37.

Nagy, D., (1966), "The Gravitational Attraction of a Right Rectangular Prism," Geophysics, 31, 362.

Nagy, D., (1967), Errata, Geophysics, 32, 368.

Press, F. and S. Biehler, (1964), "Inferences on Crustal Velocities and Densities from P Wave Delays and Gravity Anomalies," J. Geophys. Res., 69, 2979.

Rex, R. W., (1970), Investigation of Geothermal Resources in the Imperial Valley and Their Potential Value for Desalination of Water and Electricity Production, Inst. Geophys. and Planetary Phys., University of California, Riverside, Report 92502.

Richter, C. F., (1958), Elementary Seismology, W. H. Freeman, San Francisco, California, 768 pages.

Savino, J. M., T. H. Jordan, D. G. Lambert and R. C. Goff, (1976), "Passive Seismic Techniques," Systems, Science and Software Quarterly Technical Report SSS-R-77-3093 to ERDA, December 1976.

Savino, J. M., R. C. Goff, T. H. Jordan and D. G. Lambert, (1977), "Passive Seismic Techniques for Geothermal Exploration," Systems, Science and Software Quarterly Technical Report SSS-R-77-3165 to ERDA, March 1977.

Savino, J. M., R. C. Goff, W. L. Rodi, T. H. Jordan and J. H. Alexander, (1977), "Passive Seismic Techniques for Geothermal Exploration," Systems, Science and Software Quarterly Technical Report SSS-R-77-3335 to ERDA, June 1977.

Steeples, D., (1975), "Teleseismic P-Delays in Geothermal Exploration with Application to Long Valley, California," Ph.D. Thesis, Stanford University.

Wilson, J. T., (1965), "A New Class of Faults and Their Bearing on Continental Drift," Nature, 207, 343.

VI.   FISCAL INFORMATION

FISCAL STATUS REPORT

Contract No.:   E(04-3)-1313   S^3 W.O. #11050

	Cumulative to Date thru 8/31/77
COSTS INCURRED AT CONTRACTOR'S ESTIMATED INDIRECT RATES:	
Labor	49,152
Overhead 132.8%	65,274
G&A 7.6%	8,696
Computing	10,043
Travel & ODC	8,641
Total Cost	141,806
Less costs incurred in excess of contract amount	260
Fixed Fee	12,031
Total	153,577
COSTS INCURRED AT DCAA APPROVED PROVISIONAL INDIRECT RATES:	
Labor	49,152
Overhead 130.0%	63,898
G&A 8.5%	9,609
Computing	10,043
Travel & ODC	8,641
Total Cost	141,343
Fixed Fee	12,031
Total	153,374

UNITED STATES DEPARTMENT OF ENERGY
P.O. BOX 62
OAK RIDGE, TENNESSEE 37830

OFFICIAL BUSINESS
PENALTY FOR PRIVATE USE.$300

FS—   1

AMAX EXPLORATION, INC
ATTN   ARTHUR L LANGE
4704 HARLAN STREET
DENVER, CO   80212